Dalton Transactions

ROYAL SOCIETY OF CHEMISTRY

PAPER

View Article Online
View Journal | View Issue

Cite this: *Dalton Trans.*, 2025, **54**, 7221

Functional biomimetics for copper oxidases: interesting catalytic promiscuity of novel monocopper(II) complexes†

Vigneswara Chellam Ravisankar,[a] Balasubramaniam Selvakumaran,[a] Tamilarasan Ajaykamal[b] and Mariappan Murali*[a]

Employing H(L^1) [2-((pyridine-2-ylmethyl)imino)methylphenol] or H(L^2) [2-((pyridine-2-ylethyl)imino) methylphenol] and phen (1,10-phenanthroline), two novel monocopper(II) complexes, [Cu(L^1/L^2)(phen)] (ClO_4) (**1** or **2**), have been produced and studied. The single-crystal structure of the complex ion in **2**, as determined by X-ray structure analysis, shows a trigonal bipyramidal geometry with distortion (τ, 0.65). DFT calculations were used to investigate the molecular geometry of copper(II) complexes in solution as well as their electronic characteristics. The electronic and EPR spectra in the solid-state of **1** and **2** reveal a trigonal bipyramidal geometry, whereas the geometry in solution is square pyramidal. The positive and reversible nature of the redox pair (Cu^{II}/Cu^{I}) makes redox states easily interconvertible. The catalysts in methanol and/or the buffer induced three separate chemical changes: (i) ascorbic acid → dehydroascorbic acid, (ii) benzylamine → benzaldehyde, and (iii) 3,5-di-*tert*-butylcatechol → 3,5-di-*tert*-butylquinone. Their k_{cat} results show higher activities of amine oxidase (10^5 h^{-1}). Ascorbate oxidase (10^7 h^{-1}) and catechol oxidase (10^6 h^{-1}) activity in the buffer yields k_{cat} values that are closer to those of the natural enzyme. This is due to the presence of ligand flexibility, structural distortion, an appropriate chelate ring size, a labile donor, a positive redox potential, and a persistent catalyst–substrate interaction. Therefore, the two monocopper(II) complexes serve as the most efficient promiscuous catalysts, acting as complementary agents to the activity of copper oxidase enzymes and superior models for oxidation processes.

Received 11th January 2025,
Accepted 27th March 2025

DOI: 10.1039/d5dt00077g

rsc.li/dalton

Introduction

Organic synthesis relies heavily on oxidation processes, which are crucial for endowing valuable molecules with the functionality they require, like drugs, agricultural chemical products, and other valuable substances.[1–3] The perfect oxidant is molecular oxygen, which can be taken simply from the air and is both affordable and safe for the environment. Stoichiometric proportions of inorganic oxidants used in traditional oxidation processes are hazardous and contribute to contamination in the environment. For this reason, oxidations involving a catalytic dose of an activator possess the potential for activating molecular oxygen with the least amount of chemical loss. Since molecular oxygen is kinetically inert, it is difficult to make it active for applications involving oxidation processes. One of the main issues with employing dioxygen in chemical change happens to be that it is difficult to manage its reactivity, which frequently results in poor selectivity and over-oxidation.[4] Through the use of transition metals integrated into proteins, known as "metalloenzymes", nature discovered a sophisticated way to get over the kinetic hurdle of dioxygen being activated.[5,6] By developing oxygen activation catalysts, which function as miniature molecule mimics of metalloenzymes and aid in the understanding of mechanistic processes, inorganic chemists have largely capitalized on the idea of nature. The donor sites of enzymes are modeled using ligands, which are tiny molecules that are mixed with metals to generate complexes that are examined as structural and functional models. This is done by applying the understanding of coordination chemistry, electronic parameters, and redox potential.[5,7,8] The catalytic activity of the majority of metal complexes is generally quite promising. Several of these complexes would not be considered extremely effective catalysts since they cannot efficiently perform that particular organic

[a]*Coordination and Bioinorganic Chemistry Research Laboratory, Department of Chemistry, National College (Autonomous) affiliated to Bharathidasan University, Tiruchirappalli 620 001, Tamil Nadu, India. E-mail: murali@nct.ac.in, ma66mu@yahoo.co.in*

[b]*School of Chemistry, Bharathidasan University, Tiruchirappalli 620 024, Tamil Nadu, India*

†Electronic supplementary information (ESI) available. CCDC 2390596. For ESI and crystallographic data in CIF or other electronic format see DOI: https://doi.org/10.1039/d5dt00077g

oxidative reaction.[9] Despite their seeming inefficiency, several of the complexes are unquestionably very helpful in giving us invaluable knowledge into the significant mechanistic elements of the metalloenzymes. Over the past few decades, bioinorganic chemists have focused on developing catalytic reactions with the goal of comprehending and simulating the enzymatic functions of metalloenzymes.

Copper ions are essential for enzymatic catalysis of redox processes and are used by the majority of enzymes that employ molecular dioxygen. Members of copper proteins ('Type-2' and 'Type-3') that have received less attention are ascorbate oxidase (AOase), amine oxidase (AmOase), and catechol oxidase (COase). The copper site in AOase oxidizes ascorbic acid to dehydroascorbate using dioxygen. One of its three copper center types is 'Type-2' ($A_{\parallel} > 140 \times 10^{-4}$ cm^{-1}), which is part of the functional trinuclear cluster,[7,10] being coordinated to two histidine molecules and a water molecule. Electron transfer is an essential action of the 'Type-2' copper center, and ascorbate functions as an electron donor under physiological conditions of the reaction. Dioxygen is activated by the reduced copper(I) sites and transformed into water by AOase[11] using four electrons and four protons. An important two electron enzymatic process that undergoes conversion of amine to aldehyde ($RCH_2NH_2 \rightarrow RCHO + NH_3$) is the deamination reaction, which includes the 'Type-2' copper centers in AmOase.[8,12] It manifests as homodimers and exhibits a square pyramidal shape at the active site. A N_3O_2 chromophore comprising two O-donor sites[13,14] and being labile is formed by the presence of three imidazole and two water molecules at the copper(II) site. A frequently occurring enzyme in plants, insects, and crustaceans[15] is COase, a 'Type-3' copper protein. It consists of a hydroxo bridged dicopper(II) center, where each copper(II) center is coordinated by three histidine residues (two nitrogens equatorially and one nitrogen axially) and takes on a nearly trigonal pyramidal structure.[16] In the presence of dioxygen, it catalyzes the oxidation of catechol to *o*-quinone (highly reactive).[17–19] The auto-polymerization of *o*-quinone results in the synthesis of melanin. Among its various defensive functions, it protects the injured tissues from insects and pathogens.[20]

The importance of metals in a variety of biochemical reactions is the main reason for the intense interest in the production of unique metal complexes with creative structures and reactivity in diverse biological scenarios. Consequently, the structural characteristics of the metalloenzyme active sites serve as an inspiration for the molecular synthesis of several new tiny inorganic metal complexes. The fundamental objective of these complexes, which are known to be biomimetic, is to convert structural similarities with biological originals into functional ones.[21] A variety of biological activities, such as electron transport or the oxidation of different organic substrates, employ the copper ions at the active site of proteins as redox catalysts. This modeling investigation led to an important comprehension of the structural and functional characteristics of copper oxidases.[17] Even while many dicopper(II) complexes made from N/O donor dinucleating ligands are successful at replicating the structure and function of the enzyme,[18,19,22] the copper oxidase activity of numerous monocopper(II) complexes is likewise well known. The established structure-property relationships are only suitable for a limited number of molecules. In order for 'Type-2' and 'Type-3' copper oxidases to exhibit their functional characteristics during the catalytic process, it was noted that the Cu···Cu separation in dicopper(II) complexes must be smaller than 5 Å. In contrast, it is crucial to examine the oxygen transfer mechanism in AOase and AmOase using mixed-ligand monocopper(II) complexes, which provide a 4 + 1 square-pyramidal geometry that includes labile binding site(s).[20,23,24] However, for monocopper(II) complexes to become functional in COase activity, a non-planar shape about copper(II) is required.[25] The turnover numbers (k_{cat}) of the majority of the replicas are rather small in comparison with the enzymes, which is an important disadvantage of the model complexes. In light of this information, it is important to investigate whether novel varieties of monocopper(II) compounds can demonstrate copper oxidase activity in relation to the ligand flexibility, exogenous ligand type, and coordination structure surrounding the metal ion.

Enzymatic catalysis tends to be very efficient when the active site of an enzyme is accurately optimized towards a particular reaction. The ability of an enzyme to do numerous operations or enzymatic promiscuity is currently being sought after as a desirable quality since it facilitates use in biocatalysis and biotechnology. Enzymatic promiscuity encompasses three main aspects: (i) substrate: 'enzymes with a broad or relaxed specificity for substrates', (ii) condition: 'catalytic activity under different reaction conditions than those found in nature, such as high temperatures, pH levels, or anhydrous media', and (iii) catalytic promiscuity: 'enzymes that catalyze unique chemical changes with various transition states'. The two further categories of catalytic promiscuity[26] are (a) induced: 'a novel reaction arising from one or more mutations that diverge the reaction in which the wild-type enzyme was catalyzing', and (b) accidental: 'an additional reaction that the wild-type enzyme catalyzes'. However, using native enzymes can occasionally be quite costly; using functionally mimicking substances could be frequently a superior cost-effective option. As models, complexes consist of a simpler structure than enzymes and offer the potential to exhibit greater catalytic promiscuity, or the ability to facilitate a wider range of reactions through catalysis.[24,27]

In the current study, we have produced mixed-ligand, green-colored monocopper(II) complexes of the general formula $[Cu(L^1/L^2)(phen)](ClO_4)$ (1 or 2) {where $H(L^1)$ and $H(L^2)$, the Schiff bases [condensation of salicylaldehyde and 2-picolylamine, $H(L^1)$ or (2-(2-aminoethyl)pyridine), $H(L^2)$]; phen, 1,10-phenanthroline} (Scheme 1). They vary in their degree of flexibility due to changes within the chelate ring members that occur between imine and pyridine nitrogens of coordinated Schiff base ligands. Using X-ray investigations of a single crystal, we have identified the solid-state structure of **2**. The spectroscopic and electrochemical characteristics were assessed when the chelate ring members were modified from methylene (–CH_2–) to ethylene (–CH_2–CH_2–). The solution geo-

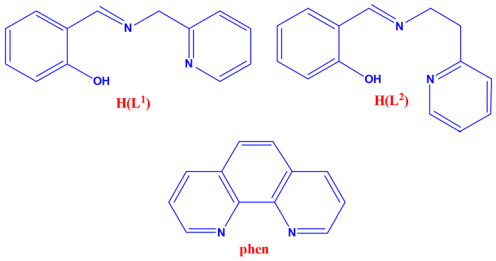

Scheme 1 Structure of ligands (tridentate NNO and bidentate NN donors).

metry of **1** or **2** was established in order to comprehend the structure–reactivity correlation. Their potential promiscuous catalytic activities have been tested through spectroscopic and electrochemical methods using a model substrate, ascorbic acid (H_2A) or benzylamine ($Ph–CH_2–NH_2$) or 3,5-di-*tert*-butylcatechol (3,5-DTBC), with the aim of mimicking the functional sites of AOase, AmOase and COase.

Experimental

Materials

Salicylaldehyde, 2-picolylamine, 2-(2-aminoethyl)pyridine, 1,10-phenanthroline, sodium perchlorate, copper(II) acetate monohydrate, 3,5-di-*tert*-butylcatechol, tetra-*N*-butylammonium perchlorate (Aldrich), potassium iodide, ammonium molybdate, hydrogen peroxide (30% w/v) solution, silica gel (Merck), L-ascorbic acid (Fisher Scientific), and benzylamine (Avra) were used as received. Disodium hydrogen phosphate (Merck), sodium dihydrogen phosphate (Merck), and NaOH (Merck) were used for the preparation of phosphate buffer solutions (pH, 5.0–8.0). Phthalate (pH, 4.0), borate (pH, 9.0) and ammonia (pH, 10.0) were obtained from SRL. Solvents like dichloromethane, methanol (HPLC), hexane, *N*,*N*-dimethylformamide, acetonitrile (HPLC), diethylether (AR), and ethyl acetate were purchased from Merck.

Buffer solutions

Phthalate (pH 4.0), phosphate (pH 5.0–8.0), borate (pH 9.0), and ammonia (pH 10.0) were used as buffer solutions to examine the pH effect. The concentration of the buffer solution was 0.1 M despite the ionic strength. Sodium phosphate monobasic and sodium phosphate dibasic were dissolved in deionized water, and the pH was then adjusted between 5 and 8 using NaOH (1 M). The final volume (250 mL) was reached by using deionized water. The buffer solution was filtered using a 0.22 μm membrane filter and kept at 4 °C before use. After being prepared and standardized, the buffer solution was used for three days. The buffer solutions used in this investigation were measured for pH using a Thermo Scientific EUTECH pH meter with an ATC electrode and a pH resolution of 0.01 for the pH range of 0 to 14. Before each set of readings, the device was calibrated using standard pH buffers (pH 4.0, 7.0, and 10.0) to guarantee accuracy. With automatic temperature adjustment enabled, all pH measurements were obtained at room temperature (25 ± 1 °C). The purchased buffer solutions were prepared using potassium hydrogen phthalate (phthalate, pH 4.0), boric acid, sodium tetraborate and sodium chloride (borate, pH 9.0), and ammonia chloride and ammonia (ammonia, pH 10.0).

Physical methods

Elements C, H, and N were analyzed using a Vario EL III elemental analyzer. Using an EQUIPTRONICS EQDCMP bridge, molar conductivity measurements in methanol were performed at 25 °C (solute concentration: 1×10^{-3} M). A JMS-T100LC spectrometer was used to record the ESI-MS spectra. An HRMS Exactive Plus EMR spectrometer was used to perform high-resolution mass spectrometry. With a PerkinElmer Spectrum Two FTIR spectrophotometer, infrared spectra were recorded in the 4000–400 cm^{-1} region using KBr pellets. A PerkinElmer Lambda 365 was used to record diffuse reflectance spectra, and a 365+ UV-VIS spectrophotometer attached to a refrigerated circulating water bath (25 ± 0.2 °C) using cuvettes (path length, 1 cm) to capture solution electronic absorption spectra in the 200–1100 nm range. The X-band EPR spectra of the solid at ambient temperature and the solution at 77 K were acquired using a JEOL JES-FA200 ESR spectrometer at an X-band frequency (9–10 GHz) with 100 kHz field modulation. A Bruker 400 MHz AVANCE III HD NMR spectrometer was used to record the ^1H NMR spectral data ($CDCl_3$) for the ligands and products separated from catalytic reactions. A CHI 620C electrochemical analyzer operating at 25 ± 0.2 °C was used to evaluate the redox potentials of copper(II) complexes **1** and **2** (0.001 M) in methanol with TBAP (0.1 M) as the supporting electrolyte. Cyclic voltammetry (CV) and differential pulse voltammetry (DPV) were employed. The standard configuration of three electrodes, such as the working electrode (glassy carbon; A, 0.0707 cm^2), counter electrode (platinum wire), and reference electrode (saturated calomel), was employed. The potential varied between −1 and +1 V at scan speeds of 0.01–0.1 V s^{-1}. Before measurements, N_2 was quickly bubbled into the solution to eliminate oxygen. Using the formula $E_{1/2} = (E_{pc} + E_{pa})/2$ and $\Delta E_p = E_{pa} - E_{pc}$, redox data have been calculated.

Synthesis of Schiff base ligands

A solution of salicylaldehyde (3.1 g, 0.025 mol) in methanol (10 mL) was added, under constant stirring, to a solution of 2-picolylamine (2.7 g, 0.025 mol) or 2-(2-aminoethyl)pyridine (3.1 g, 0.025 mol) in methanol (30 mL). The reaction mixture was refluxed at 70 °C for 2 h and cooled to room temperature. The solution was rotaevaporated to dryness, and the yellow residue was extracted with dichloromethane. The organic layer was dried over magnesium sulfate, filtered and dried in a vacuum. The residue was chromatographed through silica gel (dichloromethane : hexane = 1 : 3 v/v) to give a yellow oil of $H(L^1)$ or $H(L^2)$.

2-((Pyridine-2-ylmethyl)imino)methylphenol H(L^1). Yield: 3.3 g, 62%; ^{1}H NMR (400 MHz, $CDCl_3$) δ (multiplicity, integration, assignment) in ppm: 4.923 (s, 2H, H_8), 8.511 (s, 1H, H_7) 6.888 (d, 1H, H_2), 6.770 (t, 1H, H_3) 7.075 (t, 1H, H_4), 6.955 (d, 1H, H_5), 7.341 (d, 1H, H_{10}), 7.666 (t, 1H, H_{11}), 7.281 (t, 1H, H_{12}), 8.585 (d, 1H, H_{13}) 13.412 (s, 1H, phenolic –OH). ESI-MS: 213.2 $(M + H)^+$. Anal. found (calcd) for $C_{13}H_{12}N_2O$ (212.3): C, 73.61 (73.57); H, 5.67 (5.70); N, 13.16 (13.20).

2-((Pyridine-2-ylethyl)imino)methylphenol H(L^2). Yield: 3.6 g, 63%; ^{1}H NMR (400 MHz, $CDCl_3$) δ (multiplicity, integration, assignment) in ppm: 3.945 (t, 2H, H_8), 3.100 (t, 2H, H_9), 8.200 (s, 1H, H_7) 6.877 (d, 1H, H_2), 6.773 (t, 1H, H_3) 7.100 (t, 1H, H_4), 7.059 (d, 1H, H_5), 7.109 (d, 1H, H_{11}), 7.507 (t, 1H, H_{12}), 7.208 (t, 1H, H_{13}), 8.499 (d, 1H, H_{14}) 13.324 (s, 1H, phenolic –OH). ESI-MS: 227.4 $(M + H)^+$. Anal. found (calcd) for $C_{14}H_{14}N_2O$ (226.3): C, 74.38 (74.31); H, 6.22 (6.24); N, 12.43 (12.38).

Synthesis of copper(II) complexes

1,10-Phenanthroline (0.18 g, 1 mmol) dissolved in 10 mL of methanol was added drop by drop to a 10 mL methanol solution of copper(II) acetate monohydrate (0.20 g, 1 mmol) and stirred for 1 h at 25 °C. After the appearance of a blue solution, a 10 mL methanol solution of H(L^1) (0.21 g, 1 mmol) or H(L^2) (0.23 g, 1 mmol) was added, and the resultant green solution was refluxed for 3 h. A green crystalline precipitate formed upon the addition of 3 mL methanol solution of sodium perchlorate (0.12 g, 1 mmol). The greenish crystalline powder was collected by filtration and dried in a vacuum under pressure to give 0.32 g or 0.38 g of compound $[Cu(L^1)(phen)](ClO_4)$ (**1**) or $[Cu(L^2)(phen)](ClO_4)$ (**2**).

$[Cu(L^1)(phen)](ClO_4)$ (1). Yield: 58%. Anal. calcd for $C_{25}H_{19}N_4O_5ClCu$: C, 54.16; H, 3.45; N, 10.10%. Found: C, 54.09; H, 3.52; N, 10.18%. Λ_M: 76 (MeOH) Ω^{-1} cm^2 mol^{-1}. ESI-MS (MeCN): m/z 454.56 $[M^+ - ClO_4]$. μ_{eff} (27 °C): 1.75μ_B. FT-IR (KBr, cm^{-1}) selected bands: 1615 ν_{imine}(C=N), 1586 ν_{py}(C=N), 1228 ν(C_{ph}–O), 1090, 623 $\nu(ClO_4^-)$ 475 ν(Cu–O), 513 ν(Cu–N). Electronic spectrum in solid/MeOH [λ_{max}/nm (ε_{max}/dm^3 mol^{-1} cm^{-1})]: 709/688 (80), 932 (40), 456 sh (250), 342 (6325), 326 (10495), 295 (17870), 267 (24430). Electronic spectrum in MeOH : H_2O (4 : 1 v/v) [λ_{max}/nm (ε_{max}/dm^3 mol^{-1} cm^{-1})]: 684 (70), 931 (40), 456 sh (250), 343 (5810), 326 (10020), 321 (11500), 295 (20460), 270 (33400). Polycrystalline EPR spectrum (RT): $g_\perp$ = 2.054, $g_\parallel$ = 1.967. EPR spectrum in solution (77 K): $g_\parallel$ = 2.239, $g_\perp$ = 2.051, $A_\parallel$ = 176 × 10^{-4} cm^{-1}, $g_\parallel/A_\parallel$ = 127 cm, G = 4.7, α^2 = 0.79, β^2 = 0.66, γ^2 = 0.65, $K_\parallel$ = 0.72, $K_\perp$ = 0.65 (DMF, 1 × 10^{-2} M); g_{iso} = 2.044 (MeOH, 1 × 10^{-2} M); g_{iso} = 2.027 (MeCN, 1 × 10^{-2} M); $g_\parallel$ = 2.255, $g_\perp$ = 2.056, $A_\parallel$ = 169 × 10^{-4} cm^{-1}, $g_\parallel/A_\parallel$ = 133 cm, G = 4.5 (MeOH, 2.9 × 10^{-5} M); $g_\parallel$ = 2.264, $g_\perp$ = 2.052, $A_\parallel$ = 165 × 10^{-4} cm^{-1}, $g_\parallel/A_\parallel$ = 137 cm, G = 5.1 (buffer solution, 2.9 × 10^{-5} M). Redox behavior in MeOH (0.1 M TBAP): CV, $E_{1/2}$ = 0.045 V, ΔE_p = 90 mV, i_{pa}/i_{pc} = 1.1, D = 8.4 × 10^{-6} cm^2 s^{-1}; DPV, $E_{1/2}$ = 0.044 V. Redox behavior in aqueous MeOH (0.1 M TBAP): CV, $E_{1/2}$ = −0.028 V, ΔE_p = 83 mV, i_{pa}/i_{pc} = 1.0, D = 7.8 × 10^{-6} cm^2 s^{-1}; DPV, $E_{1/2}$ = −0.032 V.

$[Cu(L^2)(phen)](ClO_4)$ (2). Yield: 67%. Anal. calcd for $C_{26}H_{21}N_4O_5ClCu$: C, 54.93; H, 3.72; N, 9.86%. Found: C, 54.81; H, 3.78; N, 9.94%. Λ_M: 78 (MeOH) Ω^{-1} cm^2 mol^{-1}. ESI-MS (MeCN): m/z 468.66 $[M^+ - ClO_4]$. μ_{eff} (27 °C): 1.74μ_B. FT-IR (KBr, cm^{-1}) selected bands: 1624 ν_{imine}(C=N), 1588 ν_{py}(C=N), 1231 ν(C_{ph}–O), 1090, 623 $\nu(ClO_4^-)$, 463 ν(Cu–O), 515 ν(Cu–N). Electronic spectrum in solid/MeOH [λ_{max}/nm (ε_{max}/dm^3 mol^{-1} cm^{-1})]: 670/670 (100), 915 (60), 469 sh (230), 372 (6230), 295 sh, 266 (22200). Electronic spectrum in MeOH : H_2O (4 : 1 v/v) [λ_{max}/nm (ε_{max}/dm^3 mol^{-1} cm^{-1})]: 670 (90), 912 (62), 467 sh (240), 368 (6160), 294 sh, 266 (21810). Polycrystalline EPR spectrum (RT): $g_\perp$ = 2.034, $g_\parallel$ = 1.956. EPR spectrum in solution (77 K): $g_\parallel$ = 2.238, $g_\perp$ = 2.050, $A_\parallel$ = 173 × 10^{-4} cm^{-1}, $g_\parallel/A_\parallel$ = 129 cm, G = 4.7, α^2 = 0.78, β^2 = 0.66, γ^2 = 0.65, $K_\parallel$ = 0.72, $K_\perp$ = 0.65 (DMF, 1 × 10^{-2} M); g_{iso} = 2.020 (MeOH, 1 × 10^{-2} M); g_{iso} = 2.031 (MeCN, 1 × 10^{-2} M); $g_\parallel$ = 2.253, $g_\perp$ = 2.048, $A_\parallel$ = 172 × 10^{-4} cm^{-1}, $g_\parallel/A_\parallel$ = 131 cm, G = 5.3 (MeOH, 2.9 × 10^{-5} M); $g_\parallel$ = 2.253, $g_\perp$ = 2.048, $A_\parallel$ = 168 × 10^{-4} cm^{-1}, $g_\parallel/A_\parallel$ = 134 cm, G = 5.3 (buffer solution, 2.9 × 10^{-5} M). Redox behavior in MeOH (0.1 M TBAP): CV, $E_{1/2}$ = 0.044 V, ΔE_p = 88 mV, i_{pa}/i_{pc} = 1.1, D = 7.6 × 10^{-6} cm^2 s^{-1}; DPV, $E_{1/2}$ = 0.035 V. Redox behavior in aqueous MeOH (0.1 M TBAP): CV, $E_{1/2}$ = −0.073 V, ΔE_p = 106 mV, i_{pa}/i_{pc} = 1.1, D = 6.8 × 10^{-6} cm^2 s^{-1}; DPV, $E_{1/2}$ = −0.060 V.

Single-crystal X-ray structure determination

The green crystalline powder (**2**) was again dissolved in a methanol : acetonitrile mixture (1 mM solution) and taken in a test tube with diethyl ether (1 : 1, v/v) for slow evaporation at 5 °C. Suitable crystals for X-ray analysis were obtained from the solution after 8 days. A single-crystal of **2** with dimensions of 0.29 × 0.26 × 0.22 (**2**) mm^3 was selected for viewing under a polarizing microscope and mounted on glass fiber. X-ray data were collected on a Rigaku Saturn 724 CCD diffractometer with Mo-K_α radiation (λ = 0.71075 Å) at 150 K under the continuous flow of cooled nitrogen gas. The Rigaku Crystalclear software was used for data collection and integration. Absorption corrections were carried out using a multi-scan/numerical method. The crystal structure was solved by direct methods using SIR-92[28] and refined by full-matrix least-squares calculation using SHELXL version 2016/4.[29] All the calculations were carried out using the programs in the WinGX module.[30] All non-hydrogen atoms were refined anisotropically. The hydrogen atoms were refined isotropically as rigid atoms in their idealized locations. ORTEP3 software for Windows[30] was used to describe graphically the molecule using 50% probability displacement ellipsoids. The details of the crystallographic data are presented in Table 1. Crystallographic data in CIF format were deposited with the Cambridge Crystallographic Data Centre (CCDC-2390596).

Experimental procedure for ascorbate oxidase (AOase) activity

By reacting the copper(II) complexes (**1** or **2**; 3 × 10^{-3} M) and varying concentrations of ascorbic acid (H_2A), the ascorbate oxidase activity of the complexes was measured. The studies carried out under an aerobic atmosphere with a MeOH : H_2O (4 : 1 v/v) solution (**MS**) or buffer solution (**BS**)[31] were moni-

Table 1 Selected crystal data and structure refinement parameters of [Cu(L^2)(phen)](ClO_4) (**2**)

	2
Formula	$C_{26}H_{21}N_4O_5ClCu$
Formula weight	568.46
Temperature (K)	150(2)
Wavelength (Å)	0.71075
Crystal system	Monoclinic
Space group	$P2_1/n$
a (Å)	9.547(2)
b (Å)	17.906(3)
c (Å)	14.077(3)
α (°)	90
β (°)	107.131(5)
γ (°)	90
V (Å)^3, Z	2299.7(8), 4
D_{calc} (g cm^{-3})	1.642
μ (mm^{-1})	1.115
F(000)	1164
Crystal size (mm)	0.29 × 0.26 × 0.22
θ (°)	2.733–24.996
Index ranges	$-11 \le h \le 11$, $-21 \le k \le 20$, $-11 \le l \le 16$
Reflections collected	16 803
Independent reflections	4034
Reflections observed [$I > 2\sigma(I)$]	3897
R_{int}	0.0233
GOOF	1.007
R_1 [$I > 2\sigma(I)$]	0.0272
wR_2 [$I > 2\sigma(I)$]	0.0850
R_1/wR_2 all data	0.0281/0.0859

tored using UV-Vis spectroscopy. To ascertain the ascorbate oxidase activity of complexes, 60 equivalents of ascorbic acid (H_2A) were added to a 1.667×10^{-6} M complex (**1** or **2**) solution in MS (pH 7.3) or BS (pH 7.6) in an aerobic environment at 25 °C. The UV spectra of the solution were recorded at regular intervals of 1 min after the addition. Over the first 30 min, the decrease in the absorption value at ~268 nm was observed as a function of time. In an aerobic environment, the MS or BS of copper complexes (1.667×10^{-6} M) were treated with 20–140 equivalents of H_2A to ascertain the dependence of the rates on the concentration of the substrate and other kinetic parameters.[32]

Experimental procedure for amine oxidase (AmOase) activity

The conversion of benzylamine (Ph–CH_2–NH_2) to benzaldehyde (Ph–CHO) occurs as a consequence of the catalytic reaction between **1** or **2** (1×10^{-3} M) and Ph–CH_2–NH_2 (1×10^{-1} M) in 10 mL of MeOH : H_2O (4 : 1 v/v)[33] in a H_2O_2 (1 mL of 30% w/v) driven deamination process. In reactions involving Ph–CH_2–NH_2 and H_2O_2 alone or in the absence of the complex, no appreciable Ph-CHO was produced. After the methanol was removed by evaporation, diethyl ether was used as a solvent to extract organic substances from the reaction mixture. A rotary evaporator was used to remove the diethyl ether, and the residue was dissolved respectively in $CDCl_3$ and MeOH for ^{1}H NMR and HRMS analyses. Using spectrophotometry, the aqueous methanolic solution (3.3×10^{-7} M) of complexes was subjected to sequential additions of 2–12 equivalents of Ph–CH_2–NH_2 and 50 equivalents of H_2O_2. The reaction was monitored for a 60 second interval. Because of the increasing concentration of benzaldehyde (Ph–CHO), there is a progressive increase in the absorbance band at ~252 nm as the reaction proceeds. The rate of the reaction was determined using the initial rate method, and the kinetic parameters were estimated using the Michaelis–Menten approach.

Experimental procedure for catechol oxidase (COase) activity

By treating a copper(II) complex (**1** or **2**) solution (2.9×10^{-5} M) in CH_3OH (MS) or a buffer solution (BS) at pH 8.0 (**1**) or 7.8 (**2**) containing 50 (MS) or 500 (BS) equivalents of 3,5-di-*tert*-butylcatechol (3,5-DTBC) in MS or BS, the catechol oxidase activity of the complex was determined under aerobic conditions. The electronic spectra of the reaction mixture were recorded for 3 h (MS) or 30 min (BS) at a wavelength of 400 (**1**) and 390 nm (**2**) (MS) or 404 (**1**) and 399 nm (**2**) (BS). Scaling up the reactants allowed for the same reaction to be performed, and the required 3,5-di-*tert*-butylquinone (3,5-DTBQ) was extracted column chromatographically using an eluent mixture of 10% ethyl acetate and hexane. Using FTIR spectroscopy and ^{1}H NMR spectra in $CDCl_3$,[34] the isolated 3,5-DTBC was found. It became apparent that the rates and kinetic parameters of the complexes (MS, 2.9×10^{-5}; BS, 2.9×10^{-6} M) under aerobic conditions depended on the substrate concentration (MS, 10–60 or BS, 100–700 equivalents).[35] As buffers, ammonia (pH 10.0), borate (pH 9.0), phosphate (pH 5.0–8.0), and phthalate (pH 4.0) were used to study the pH effect. The buffer, complex, and substrate concentrations in the absence of ionic strength were [buffer] = 0.1 M, [complex] = 2.9×10^{-5} M, and [3,5-DTBC] = 1.45×10^{-3} M. The reaction mixture used to produce hydrogen peroxide catalytically was made in the same way as kinetic experiments. The pH of the reaction mixture was lowered to 2 with H_2SO_4 and an equivalent amount of water to cease the oxidation reaction. The formed quinone was extracted three times with dichloromethane. To the aqueous layer were added 1 mL of a 10% solution of KI and three drops of a 3% solution of ammonium molybdate. Spectrophotometric monitoring of the formation of I_3^- was done using the development of a typical I_3^- absorption band at ~353 nm (ε, 26 000 M^{-1} cm^{-1}).[36]

Please refer to the ESI† for details of the computational protocol.

Results and discussion

Synthesis and general aspects

Copper(II) acetate monohydrate [$Cu(O_2CMe)_2 \cdot H_2O$] was reacted with a Schiff base H(L^1) or H(L^2) (obtained *via* condensing 2-picolylamine or 2-(2-aminoethyl)pyridine with salicylaldehyde), phen (1,10-phenanthroline), and $NaClO_4$ in methanol at a refluxing temperature to generate monocationic copper(II) complexes (**1** or **2**). At ambient temperature, the two complexes were stable in air after being separated into a crystalline substance in moderate to high yields (**1**, 58; **2**, 67%). The molar conductivities (Λ_M) of complexes **1** and **2** were determined to

be 76 and 78 Ω^{-1} cm^2 mol^{-1} in methanol solutions (1.0×10^{-3} M), accordingly. The predicted formulas, which show a 1 : 1 electrolytic nature, are completely in line with these values.[37,38] They exhibited solubility in methanol (MeOH) and acetonitrile (MeCN), as evidenced by their solution molar conductivity measurements over a period of four days, which revealed no indications of degradation or solvolysis. The stability and purity of Cu(II) complexes are shown by the ESI mass spectra in MeCN solution. The molecular mass detected, with an *m*/*z* value of 454.56 (**1**) or 468.66 (**2**), is consistent with the formula of the molecular ion peak [$M^+ - ClO_4$]. Since the two copper(II) complexes exhibit stretching vibrations associated with $\tilde{\nu}_{imine}$(C=N) [1615 (**1**); 1624 cm^{-1} (**2**)], $\tilde{\nu}_{py}$(C=N) [1586 (**1**); 1588 cm^{-1} (**2**)], and $\tilde{\nu}$(C_{ph}–O) [1228 (**1**); 1231 cm^{-1} (**2**)], which show that nitrogen (amine and pyridine) and oxygen (phenolate) donors are coordinated to copper(II), and their spectral patterns are comparable. The existence of a significant absorption for the ClO_4^- stretching vibrations at 1090 and 623 cm^{-1} indicated the emergence of a monocationic copper(II) complex. The two sharp bands were noticed (**1**, 475, 513; **2**, 463, 515 cm^{-1}) due to the result of ligand coordination and are caused by the $\tilde{\nu}$(Cu–O) and $\tilde{\nu}$(Cu–N) stretching.[39,40] It becomes apparent that at 27 °C, the effective magnetic moment (μ_{eff}) value is 1.75 (**1**) or 1.74μ_B (**2**). This result coincides with the predicted spin-only magnetic moment for an electronic system [S = 1/2, Cu(II) d^9].[41] Using elemental analysis, the general form of the complexes, [Cu(L^n)(phen)](ClO_4) (**1** or **2**), was established, which is compatible with the single-crystal X-ray structure of **2**.

Single crystal X-ray structure of [Cu(L^2)(phen)](ClO_4) (2)

The monocationic [Cu(L^2)(phen)](ClO_4) (**2**) is shown in an ORTEP image (Fig. 1a), together with the atom numbering system. All selected bond lengths and angles are listed in Table 2. The anionic Schiff base ligand H(L^2), which is tridentate in the cationic portion, facially coordinates with the central Cu(II) ion through one phenolate oxygen and one imine and one pyridine nitrogen atoms. The most accurate description of the coordination polyhedron the Cu(II) center is that it is severely distorted trigonal bipyramidal. The potential source of the perfect geometrical distortion could be the asymmetric and non-planar Schiff base, resulting in the formation of two six-membered chelate rings. Due to the sp^3 and sp^2 hybridizations of the carbon atoms in the chelating ligand, the six-membered chelate rings of the Schiff base [N(4)–C(17)–C(18)–C(19)–N(3) and N(3)–C(20)–C(21)–C(26)–O(1)] are puckered. The bidentate 1,10-phenanthroline (phen) and the tridentate Schiff base [H(L^2)] are chelating through three pyridine [N(1), N(2), N(4)] and one imine [N(3)] nitrogens and one phenolate oxygen [O(1)] in the central metal coordination sphere. For Cu(II), this coordination is typical of either a square pyramidal (sp) or trigonal bipyramidal (tbp) geometry. There have been reports of some compounds recently where the Cu(II) ion takes on a geometry somewhere between sp and tbp.[42,43] A trigonal index value (τ_5), defined as $\tau = (\beta - \alpha)/60$, where β is the highest coordination angle and α is the second biggest, has been introduced by Addison *et al.*[44] as a means of differentiating between a tbp and an sp geometry in five-coordinate metal complexes. Typically, a perfect square pyramidal geometry is

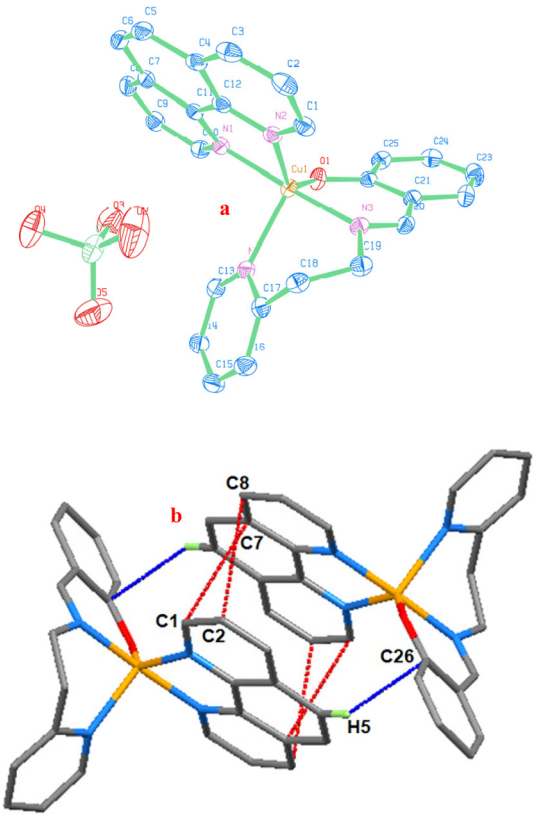

Fig. 1 (a) ORTEP image of [Cu(L^2)(phen)](ClO_4) (**2**) showing 40% probability thermal ellipsoids with atom labeling for the metal and heteroatoms. (b) Packing diagram seen along the *a*-axis exhibiting intermolecular interactions of [Cu(L^2)(phen)]$^+$: (i) red, π···π stacking and (ii) blue, C–H···π (symmetry code: $-x + 1/2$, $y + 1/2$, and $-z + 1/2$).

Table 2 Bond lengths (Å) and bond angles (°) of copper(II) complexes

	X-ray	DFT[a]	
	2	**2**	**1**
Cu(1)–N(1)	2.0130 (16)	2.096	2.077
Cu(1)–N(2)	2.1335 (15)	2.143	2.102
Cu(1)–N(3)	1.9634 (15)	2.011	1.978
Cu(1)–N(4)	2.1750 (15)	2.372	2.344
Cu(1)–O(1)	1.9481 (13)	1.946	1.940
O(1)–Cu(1)–N(1)	87.78 (6)	84.947	81.021
O(1)–Cu(1)–N(2)	138.10 (6)	153.457	161.731
O(1)–Cu(1)–N(3)	93.20 (6)	92.398	92.517
O(1)–Cu(1)–N(4)	111.83 (6)	107.800	108.607
N(1)–Cu(1)–N(2)	79.79 (6)	75.398	76.392
N(1)–Cu(1)–N(3)	177.04 (6)	174.889	174.319
N(1)–Cu(1)–N(4)	95.29 (6)	92.172	95.955
N(2)–Cu(1)–N(3)	97.65 (6)	96.889	95.714
N(2)–Cu(1)–N(4)	109.08 (6)	101.768	102.547
N(3)–Cu(1)–N(4)	86.93 (6)	91.971	88.927

[a] Calculated from the B3LYP level of theory with mixed basis sets LANL2DZ/6-31G* using methanol as a solvent employing the CPCM method.

denoted by τ = 0 and an ideal trigonal bipyramidal geometry by τ = 1.[44] Here, the compromise between tbp and sp structures may better characterize the geometry surrounding the central copper atom (τ = 0.65 for **2**). Stated otherwise, the complex ion displays a highly distorted (3 + 2) (NNO + NN) trigonal bipyramidal geometry surrounding the metal center, corresponding to the CuN_4O chromophore coordination mode.

The mean basal triangular plane is shared by one phenolate oxygen atom O(1) and one pyridine nitrogen atom N(4) of H(L^2), as well as one pyridine nitrogen atom N(2) of phen. The distances between Cu(1)–N(1), Cu(1)–N(2), Cu(1)–N(3), Cu(1)–N(4) and Cu(1)–O(1) are 2.0130(16), 2.1335(15), 1.9634(15), 2.1750(15), and 1.9481(13) Å, respectively. To put it another way, axial nitrogen bond lengths are marginally smaller than equatorial nitrogen bond lengths. The bond angles are 109.08(6), 111.83(6), 138.10(6), and 177.04(6)° for the equatorial N(4)–Cu(1)–N(2), N(4)–Cu(1)–O(1), N(2)–Cu(1)–O(1), and axial N(3)–Cu(1)–N(1). The Cu(II) center deviates by 0.116(13) Å in the direction of N(1) from the mean basal plane formed by N(2), N(4), and O(1). The axial–equatorial bond angles show the deviation from the trigonal pyramidal geometry; they range from 79.79(6) to 97.65(6)° from a typical value of 90°. At the copper center, there is a little twist in the H(L^2) ligand. Torsion angles of two six-membered chelate rings, which differ significantly from normal *gauche* and *trans* angles, appear to indicate strain. The values in analogous pentacoordinated complexes published elsewhere in the literature[42,43,45,46] are in close agreement with the bond angles and bond lengths of **2**.

Numerous non-covalent interactions (hydrogen bonding, π···π stacking, cation–π, anion–π, and C–H···π), in the crystal packing of compounds, stabilize solid state crystal structures.[47,48] The cations of neighboring molecules in the crystal packing of **2** are grouped in dimeric association (Fig. 1b) as a result of attractive C–H···π and inter-pair π···π non-covalent interactions. The interaction between the phenyl ring of phen and the phenyl ring of H(L^2) is the most significant intermolecular interaction, and it is represented by the C–H···π interaction [distance of H(5)···Cg(ph) is 2.640 Å; ∠C(5)–H(5)···Cg(ph) is 164.26°].[49] Through antiparallel stacking interactions between the coordinated pyridine rings, it forms a dimer along the *a* axis of the unit cell. Specifically, it does so between the following coordinated pyridine rings: (i) C(2) of py and C(8) of py (distance of C(2)···C(8) is 3.389 Å), and (ii) C(1) of py and C(7) of py (distance of C(1)···C(7) is 3.297 Å). The coordinated phen ligands have a plane-to-plane distance of 3.309 Å, whereas the distance of Cg(py)···Cg(py) is 3.624 Å.[50] These two interactions demonstrate a Cu···Cu distance of 7.040 Å and stabilize the structure of **2**. They also show the nearby approach and orientation of the adjacent molecules.

DFT analysis of structural and electronic properties

Using the density functional theory (DFT) approach in methanol medium, geometry optimization for **1** and **2** was shown to have no negative Eigen value (Fig. 2), indicating structural stability. Quantitative examination of the geometry and

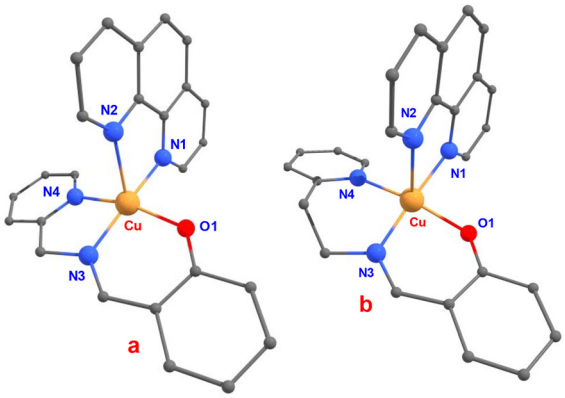

Fig. 2 DFT optimized structures of complexes [Cu(L^1)(phen)]$^+$ **1** (a) and [Cu(L^2)(phen)]$^+$ **2** (b).

ground electronic characteristics of the compounds is made possible by optimization of the molecular orbital geometry. Employing the B3LYP and 6-31G*/LANL2DZ levels and the Gaussian 09 computer program,[51] the optimized energies, frontier molecular orbital (FMO), and highest occupied molecular orbital (HOMO)–lowest unoccupied molecular orbital (LUMO) energy gaps have been determined. Bond length and bond angle calculations were made using geometry optimization, and the experimental values of **2** from single-crystal X-ray studies were compared with the calculated values (Table 2).

The calculated bond lengths of Cu–N3 (0.048 Å) and Cu–N4 (0.197 Å) are longer, Cu–O1 is comparable, and Cu–N1 (0.083 Å) is shorter at the basal plane while Cu–N2 (0.009 Å) is longer at the axial position. Even so, the calculated structural parameters for **2** well match those seen in its X-ray crystal structure. Although the bond angles in the crystal are 177.0° and 138.1°, the two longest calculated bond angles, N1–Cu–N3 and N2–Cu–O1, diverge from an ideal 180° by 174.9° and 153.5°, respectively. The calculated bond lengths and bond angles are nearly identical in the optimized structures of **1** and **2**. As a result, the geometry of the optimized structure in **1** differed slightly from that in **2**. Two longer estimated bond angles were used to determine the trigonality index (τ)of **1** (0.21) and **2** (0.36). The geometry of the copper center in **1** and **2** is distorted square pyramidal, and τ for **2** differs from the experimental result (τ, 0.65). Therefore, in contrast to the experimental geometry of **2** in the solid-state, the optimized structures of **1** and **2** are altered in the solution-state (methanol medium). The experimental electronic and EPR spectral results in methanol (*cf.* below) substantiate it. Moreover, the planar phen ligand coordinated axially (N2) and equatorially (N1) and L^1 or L^2 (N3, N4, O1) coordinated equatorially in a 4 + 1 manner with the Cu(II) cation is enforced by the lower twist angle between the O–Cu–N and N–Cu–N planes, estimated for **1** and **2**, being similar (1.2) in the solution state. It leaves a positive effect on the ease of a labile oxygen donor and a continuous catalyst–substrate interaction, which results in efficient catalytic activity.

The FMOs (HOMO, HOMO+1, LUMO, LUMO−1) define the manner in which a particular molecule interacts with other species and are essential to regulating a wide range of molecular chemical reactions.[52] The capacity of a compound to donate an electron is determined by its E_{HOMO}, whereas its capacity to accept an electron is determined by its E_{LUMO}. These MOs are significant because they use HOMO–LUMO priority orbitals to interact with other molecules. An essential foundation for assessing the stability, chemical reactivity, and selectivity of the complexes is provided by the analysis of orbital distribution, which frequently portrays the capacity of electrons to migrate from the occupied to the unoccupied orbitals.[53] While the unoccupied (LUMO) orbitals were positioned on the pyridine and imine nitrogens, the phenolate oxygen of L^1 or L^2, and the equatorial nitrogen of phen coordinated to Cu(II) in the square plane of **1** or **2**, the occupied (HOMO) orbitals were situated on the imine-phenolate unit of L^1 or L^2 and the axial nitrogen of phen (Fig. 3). There is a significant energy difference between E_{LUMO+1} and E_{LUMO}; the LUMO has around 1.5 times the value of the LUMO+1, indicating high-energy transition from the LUMO+1 to the LUMO. On the other hand, E_{HOMO-1} and E_{HOMO} values are comparable, indicating that these orbital transitions differ very little (Table 3). Research has demonstrated that, in contrast to compounds with lower E_{HOMO} values, those with higher E_{HOMO} values readily donate electrons.[54]

We anticipate a beneficial interaction since the electron donation of the complexes with another chemical system is plausible, as indicated by the relative E_{HOMO} value of −5.8 eV found in this computation. According to these findings, more energy is involved in the electron transition in the HOMO than in the LUMO. Several characteristics of quantum chemistry including the ionization potential (IP = $-E_{HOMO}$),[53] electron affinity (EA = $-E_{LUMO}$),[53] band gap ($\Delta E = E_{LUMO} - E_{HOMO}$), chemical hardness ($\eta = E_{LUMO} - E_{HOMO}/2$),[55] global softness ($S = 1/\eta$),[55] electrochemical potential ($\mu = -(IP + EA)/2$),[56] electrophilicity index ($\omega = \mu^2/2\eta$),[57] and electronegativity ($\chi = -\mu$)[56] were computed. Theoretical understanding of chemical reactivity and selectivity is largely dependent on these electronic characteristics (Table 3). The electronic characteristics of **1** and **2** are comparable because they are analogous. The nucleophilic characteristics and electron-withdrawing capacity of the complexes are apparent in the quantities IP and EA, which are obtained from E_{HOMO} and E_{LUMO}, respectively. In particular, EA has proven to be a useful characteristic for determining the rate of electron transfer from $O_2^{\bullet-}$ to Cu(II) ions and evaluating copper oxidase activity.[58] There was a noticeable amount of copper oxidase activity because the complexes with lower EA values carried more electrons during the transfer. The energy difference between the E_{HOMO} and E_{LUMO}, or the band gap (ΔE), is one of the most crucial stability factors for assessing electron conductivity and molecular reactivity. The calculated ΔE values of **1** and **2** are relatively low, 0.91 and 1.03 eV, respectively; stability and reactivity have been attributed to low ΔE values.[57,59] The computed values indicate the possible ease of reactivity in these complexes, and the most advantageous parameters are ΔE, η, and S. The complexes show electrophilic behavior[57] with a higher ω index. Due to the positively charged coordinating metal (Cu), we observed a lower electronegativity (χ) power for the structures.

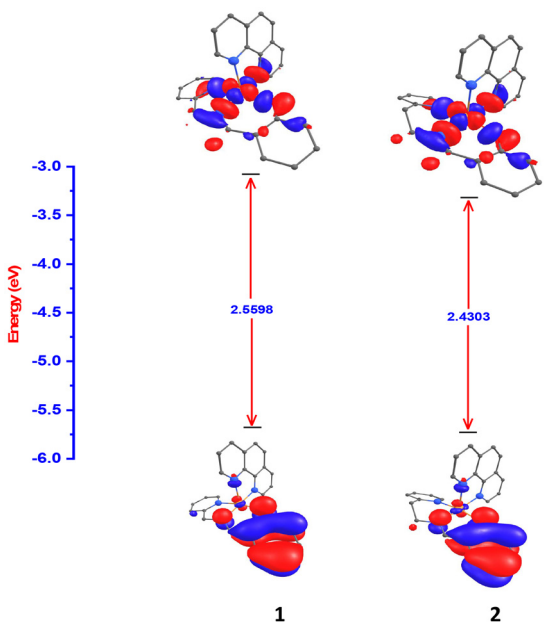

Fig. 3 Energy profile diagram of complexes $[Cu(L^1)(phen)]^+$ **1** (a) and $[Cu(L^2)(phen)]^+$ **2** (b). The doublet spin state: HOMO and LUMO in restricted spin calculations were carried out using the B3LYP level of theory with mixed basis sets LANL2DZ/6-31G* using methanol as a solvent employing the CPCM method.

Table 3 Quantum chemical descriptors for the copper complexes at the B3LYP /LANL2DZ/6-31G* level of theory using methanol as a solvent employing the CPCM method

Energy (eV)	1	2
Optimized energy (× 10^4)	−3.9577	−4.0647
HOMO	−5.7569	−5.7509
HOMO−1	−5.8159	−5.8004
LUMO	−3.1971	−3.3206
LUMO+1	−2.2831	−2.2885
Energy gap, ΔE (eV)	2.5598	2.4303
IP (eV)	5.7569	5.7509
EA (eV)	3.1971	3.3206
μ (eV)	−4.4770	−4.5358
η (eV)	1.2799	1.2152
S (eV^{-1})	0.7813	0.8229
ω (eV)	7.8301	8.4651
χ	4.4770	4.5358

Spectral and electrochemical properties

One broad ligand field absorption band is visible in the solid state reflectance spectra (Fig. S1 and S2†) of complexes **1** (709 nm) and **2** (670 nm). However, in methanol solutions, two well-separated (>3000 cm^{-1}) d–d bands with an approximate 2 : 1 intensity ratio are observed at 688 nm (ε_{max}, 80 M^{-1} cm^{-1}) and 932 nm (ε_{max}, 40 M^{-1} cm^{-1}) (**1**) or 670 (ε_{max}, 100 M^{-1}

cm^{-1}) and 915 nm (ε_{max}, 60 M^{-1} cm^{-1}) (**2**) (Fig. S3 and S4†). This suggests that the complexes undergo a change in dissolution[60–62] with the geometry changing from a trigonal bipyramidal component[63] revealed in the X-ray structure of **2** to a square-derived component with significant axial interaction. Also, because of the phenolate oxygen and nitrogen coordinations to copper(II), which correspond to phenolate-to-Cu(II) and N(π)-to-Cu(II) ligand-to-metal charge-transfer (LMCT) transitions, they show an intense shoulder at 456 nm (ε_{max}, 250 M^{-1} cm^{-1}) (**1**) or 469 nm (ε_{max}, 230 M^{-1} cm^{-1}) (**2**) and a band at 342 nm (ε_{max}, 6325 M^{-1} cm^{-1}) (**1**) or 372 nm (ε_{max}, 6230 M^{-1} cm^{-1}) (**2**), respectively. This is in accordance with the coordination sphere of five-coordinate copper(II) complexes stabilizing in solution, which is more inclined toward a square pyramidal geometry than a trigonal bipyramidal geometry.[64] The bands in the 266–295 nm region are caused by the intraligand transitions of phen, while the high intensity bands at 326 nm are attributed to the π–π* transitions of L^1 (it is not noticeable in L^2). The complexes in MeOH : H_2O (4 : 1 v/v) solutions show a comparable spectral pattern in the UV-visible spectral measurements (Fig. S5 and S6†), indicating no change in the coordination sphere.

The polycrystalline EPR spectra of **1** and **2** are identified by two *g* values (Fig. S7 and S8†). Two possible alternate geometries for Cu(II)-pentacoordinated complexes are as follows: one approaches the trigonal bipyramidal, while the other approaches the limit of square pyramidal. The two conditions are distinguished by EPR spectroscopy.[65] In addition to demonstrating an axial symmetry with two *g* values [$g_\perp$: 2.054 (**1**) and 2.034 (**2**); $g_\parallel$: 1.967 (**1**) and 1.956 (**2**)], the spectra of the complexes support the former geometry. The *g* factor corresponding to the higher symmetry axis ($g_\parallel$) is nearly coincident with g_e (2.0023). A pentacoordinate arrangement strongly shifted toward the trigonal bipyramidal[60,66,67] is indicated by the relations $g_\perp > g_\parallel$ and $g_\parallel \approx g_e$. While the pyridine nitrogen atom (phen) and the imine nitrogen atom [$H(L^n)$] occupy the two axial positions, the equatorial plane is occupied by pyridine nitrogen and phenolate oxygen atoms [$H(L^n)$] and a pyridine nitrogen atom (phen) (*cf.* above).

The axial pattern with a weakly resolved parallel feature is apparent in the frozen solution (77 K) EPR of **1** or **2** (Fig. S9 and S10†). The four parallel hyperfine patterns were well separated in DMF (conc. 1×10^{-2} M), which is ascribed to the interaction with copper nuclei in the parallel region. In contrast, they exhibit an isotropic pattern, with a perpendicular feature in MeOH (g_{iso}: **1**, 2.044; **2**, 2.020) and MeCN (g_{iso}: **1**, 2.027; **2**, 2.031) being noticeably broader (conc. 1×10^{-2} M). In diluted MeOH [conc. 2.9×10^{-5} M; $g_\parallel$: 2.255 (**1**), 2.253 (**2**); $g_\perp$: 2.056 (**1**), 2.048 (**2**)] and buffer solutions [conc. 2.9×10^{-5} M; $g_\parallel$: 2.264 (**1**), 2.253 (**2**); $g_\perp$: 2.052 (**1**), 2.048 (**2**)] the four parallel hyperfine signals were clearly discernible (Fig. S11–S14†). This implies that regardless of solution concentration, solvolysis[68] breaks the intermolecular dimeric interaction in a strong coordinating DMF solvent. However, in a weak coordinating MeOH solvent, the broadening at a high concentration is caused by the near proximity of many monomers, as it was not observed at low concentrations. The derived values of $g_\parallel$ (**1**, 2.239; **2**, 2.238) and $g_\perp$ (**1**, 2.051; **2**, 2.050) are consistent with the EPR spectra in DMF, which show absorption characteristics for the mononuclear species and belong to an axially elongated tetragonal stereochemistry. The unpaired electron in these complexes is found in the $d_{x^2-y^2}$ orbital of the copper(II) ion, which is situated in square-based geometries, as indicated by the trend $g_\parallel > g_\perp > g_e$ (2.0023).[40] In both instances, the measured $g_\parallel$ is less than 2.3, indicating that the copper complexes appear to be covalent in character.[69] Additionally, they demonstrate that $g_\parallel$ = 2.238 or 2.239, which is consistent with these chelates possessing mixed copper–oxygen and copper–nitrogen bonds.[70] At a low field, $A_\parallel$ (**1**, 176; **2**, 173 × 10^{-4} cm^{-1}) values ranged from 2600 to 3600 Gauss, indicating hyperfine splitting. However, the perpendicular region is not affected by the superhyperfine splitting brought on by the interaction with the nitrogen-donating ^{14}N (I = 1) ligand. Around 2.200 and 200 × 10^{-4} cm^{-1}, respectively, are the $g_\parallel$ and $A_\parallel$ values for the CuN_4 chromophore[71,72] in a square planar geometry. The $g_\parallel$ value decreases and the $A_\parallel$ value increases when oxygen donors are substituted for nitrogen donors. Alternatively, the $g_\parallel$ and $A_\parallel$ values for a CuO_4 chromophore[73] are about 2.420 and 145 × 10^{-4} cm^{-1}, respectively. A strong axial interaction with the CuN_3O chromophore based on a square is thus consistent with the observed $g_\parallel$ and $A_\parallel$ values. Conversely, decreased $A_\parallel$ values of the complexes most likely indicate that the copper environment is distorted. Higher $g_\parallel/A_\parallel$ values (**1**, 127; **2**, 129 cm) reflect a structural distortion in the CuN_3O chromophore based on a square.[74] The *G* value (4.7) ruled out the exchange interaction that takes place between the copper (II) centers for these complexes.[75] However, these spectral characteristics along with the positioning of the d–d absorption reveal a square pyramidal structure with a CuN_4O chromophore, in which the nitrogen atom engages the axial position while three nitrogens and oxygen choose the equatorial plane. Bonding characteristics of the complexes, including in-plane π-bonding (β^2, covalent) and in-plane σ-bonding (α^2, between ligand and 3d orbitals) have been identified.[76] According to the values of β^2 (**1** or **2**, 0.66) and α^2 (**1**, 0.79; **2**, 0.78), the π-bonding is more covalent than the σ type and σ-bonding has an ionic character. The bonding between the ligand and copper(II) ion is quite covalent, as indicated by the β^2 values. Significant out-of-plane π-bonding is revealed by the orbital reduction factor,[77] $K_\parallel$ (0.72) > $K_\perp$ (0.65).

Using cyclic voltammetry (CV) and differential pulse voltammetry (DPV), the electrochemical behavior of **1** or **2** (0.001 M complex; 0.1 M supporting electrolyte, NBu_4ClO_4; working electrode, glassy carbon; and medium, CH_3OH) was examined (Fig. S15–S18†). Upon scanning negatively, both complexes exhibit a reversible redox event during reduction, which was associated with the Cu(II) → Cu(I) reduction process. One reversible oxidation peak appeared as a result of the Cu(I) → Cu(II) oxidation process while scanning positively after cycling back. The copper(II) complexes that contain the CuN_4O chromophore are compatible with the $E_{1/2}$ values (**1**, 0.045; **2**, 0.044 V *vs.* SCE). The Cu^{II}/Cu^{I} redox behavior is both chemi-

cally and electrochemically reversible, as shown by the linear plot of i_{pc} *versus* $\nu^{1/2}$ [D, 8.4 (**1**), 7.6 × 10^{-6} cm^2 s^{-1} (**2**)] and the peak current ratio [i_{pa}/i_{pc}, 1.1 (**1**); 1.1 (**2**)]. Under the same conditions of an experiment, the limiting peak-to-peak separation of the Fc/Fc^+ couple (ΔE_p, 86 mV; $E_{1/2}$, 0.406 V *vs.* SCE) is substantially closer to the value of complex **1** or **2** [ΔE_p, 90 (**1**) or 88 mV (**2**)]. In reality, a number of factors affect the molecular structure of the complexes, which in turn regulates the redox potential of the Cu(II)/Cu(I) pair. These factors include the size of the chelate ring, axial ligation, degree and distribution of unsaturation, and substitution pattern within the chelate ring.[78] However, **1** and **2** are varied by the chelate ring size (**1**, 655; **2**, 665 chelate rings), and they display similar $E_{1/2}$ and ΔE_p, confirming the influence of structural distortion on the redox potential. This suggests that both are more appropriate for the easy inter-conversion of the tetrahedral (Cu^I) to the square planar (Cu^{II}) geometry due to the structural distortion. It is suggested that during the heterogeneous electron transfer process in **1** or **2**, between copper(II) and copper(I) species, the coordination sphere experiences a minimal amount of stereochemical reorganization.[79] This could be attributed to the flexible equatorial phenolate oxygen coordination. These findings are in line with the structural distortion of the CuN_3O chromophore based on a square in **1** or **2**, which are higher values of the $g_{\|}/A_{\|}$ index (*cf.* above) and represent intermediate geometric features between Cu(II) and Cu(I) redox-active states.

Oxidation of ascorbic acid (H_2A) to dehydroascorbic acid (DA)

By reacting with **1** or **2** (3.0 × 10^{-3} M) and varying concentrations of ascorbic acid (H_2A) in aqueous methanol under aerobic conditions at 25 °C, the ascorbate oxidase activity of the complexes was assessed (Fig. 4 and Fig. S19†). The original green solution, attributed to the Cu(II) complexes, changed to a brown solution (Fig. 4b–e and Fig. S19b–e†) upon the immediate addition of the substrate, H_2A, to the catalyst (**1** or **2**) solution. A new charge transfer (CT) band at 437 (**1**) or 434 nm (**2**) is observed up to 15 min (inset in Fig. 4 and Fig. S19†), which may be the result of Cu(II) converting to Cu(I) species.[80,81] When exposed to air, the brown colour of the solution changes to green within 20 to 30 min of time (Fig. 4f–4h and Fig. S19f–19h†). This occurs simultaneously with the disappearance of the CT band and the reappearance of the d–d band, indicating the transformation of the reduced species, Cu(I), into the oxidized form, Cu(II), using dioxygen as an oxidant. The parent copper(II) species regenerates, resulting in an isosbestic point at either 649 (**1**) or 644 (**2**) nm. It becomes apparent that the catalytic cycle of **1** or **2** (Scheme 2) is efficient at a [H_2A] : [complex] molar ratio of almost 100 : 1 (**1**) or 130 : 1 (**2**).

Using the initial rate approach, the kinetics of H_2A oxidation in aqueous methanol solution (pH 7.3) MS or buffer solution (pH 7.6) (Fig. S20–S22†) BS was ascertained by tracking the decrease in the absorption band at ~268 nm over the course of the first 30 minutes (Fig. 5 and Fig. S23, S24†). The decrease in the absorbance of H_2A suggests that it is being oxidized in the presence of the copper(II) complex to generate DA. The rate constant data demonstrate considerable reactivity differences and ascorbate oxidase activity. Under aerobic conditions, solutions of copper complexes were treated with various concentrations of H_2A (20–140 equivalent) to examine the influence of rates on the substrate concentration and other kinetic parameters. At low concentrations of H_2A, first-order dependence of the substrate concentration was found, with the effect being more pronounced for **2** than **1**. Both complexes displayed saturation kinetics at higher concentrations. The dependence on the substrate concentration shows that the catalyst–substrate interaction is an early step in the catalytic process.

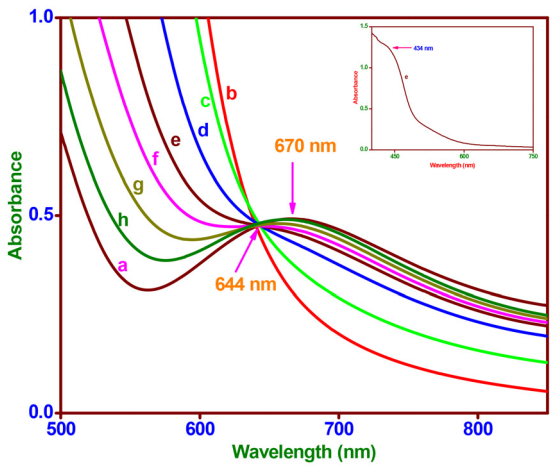

Fig. 4 Spectral trace of $[Cu^{II}(L^2)(phen)]^+$ (**2**, 3 × 10^{-3} M) in MeOH : H_2O (4 : 1 v/v) in the visible region (spectrum a); reduction of copper(II) to copper(I) (color change from green to brown) with addition of H_2A (3 × 10^{-3} M) up to 15 min (spectra b, c, d, and e); regeneration of copper(II) species (color change from brown to green) from 20 to 30 min (spectra f, g, and h). Inset: generation of charge transfer band in brown solution due to formation of copper(I) species up to 15 min (spectrum e).

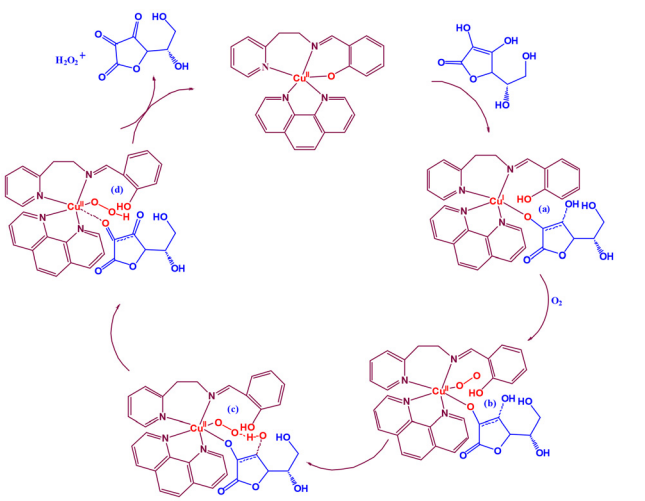

Scheme 2 Based on experimental results, the possible catalytic cycle for the oxidation of H_2A to DA {catalyst, $[Cu(L^2)(phen)]ClO_4$ (**2**)}.

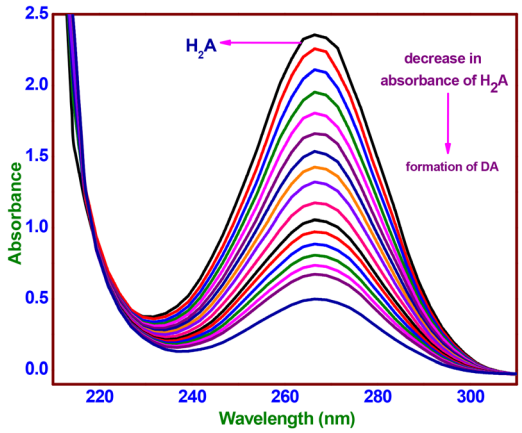

Fig. 5 Oxidation of ascorbic acid by [Cu(L^2)(phen)](ClO$_4$) (**2**) in buffer solution (pH 7.6) monitored by UV-Vis spectroscopy.

The rates of reactions measured at various H_2A concentrations were fitted to the Michaelis–Menten equation and linearized employing the Lineweaver–Burk plot (Fig. 6 and Fig. S25–S27†) to derive important kinetic parameters such as the maximum rate of the reaction (V_{max}) [MS, 22.2 (**1**) or 39.1 × 10^{-4} Ms^{-1} (**2**); BS, 23.1 (**1**) or 47.8 × 10^{-4} M s^{-1} (**2**)], Michaelis binding constant (K_M) [MS, 1.0 (**1**) or 3.1 × 10^{-4} M (**2**); BS, 0.2 (**1**) or 0.4 × 10^{-4} M (**2**)] and turnover number (k_{cat}) [MS, 4.8 (**1**) or 8.5 × 10^6 h^{-1} (**2**); BS, 2.5 (**1**) or 5.2 × 10^7 h^{-1} (**2**)]. The complexes are highly effective at oxidizing H_2A in the presence of molecular oxygen, resulting in DA. The reaction kinetics clearly indicate that a stable copper(II) complex–substrate adduct is present. Control experiments demonstrated that the desired DA product did not develop in an inert environment. Therefore, the copper(II) complex catalyzes the synthesis of DA in the catalytic process that proceeds from H_2A oxidation that involves molecular oxygen. The ascorbate oxidation feature of the Cu(II) sites in AOase is modeled by the catalytic activity of the complexes in the ascorbate oxidation by molecular oxygen involving the reduced copper(I) intermediate.

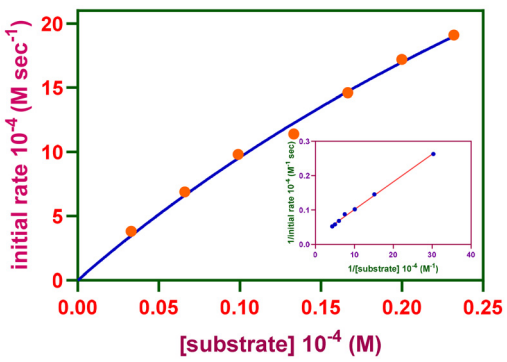

Fig. 6 Reaction rates of the oxidation reaction catalyzed by [Cu(L^2)(phen)](ClO$_4$) (**2**) in buffer solution (pH 7.6) depending on the ascorbic acid content. Inset: Lineweaver–Burk plot.

The chemical conversion of H_2A to DA was investigated by means of a cyclic voltammetric (CV) experiment (Fig. 7) with catalyst **2** (complex **2**:H_2A; molar ratio, 1 : 5) without the purging of the nitrogen gas at ten-minute intervals. In the CV of complex **2**, which was acquired at a scan rate of 50 mV s^{-1}, one reduction wave and one matching oxidation wave were detected at −0.125 V (i_{pc}, 6.1 μA) and −0.019 V (i_{pa}, 4.0 μA), respectively. The obtained current functions agree with a one-electron Cu^{II}/Cu^{I} redox pair (Fig. 7a), where the $E_{1/2}$ value is −0.053 V (ΔE_p, 106 mV). The complex solution exhibits a reduction in $E_{1/2}$ of −0.067 V (ΔE_p, 133 mV) upon the addition of H_2A, indicating a Cu^{I}/Cu^{II} pair redox mechanism. The addition of H_2A rapidly reduces Cu(II) to Cu(I), and at the same time, it generates a five-coordinate complex-monodehydroascorbate adduct {[(phen)(HL^2)-Cu^{I}-(HA)]}, which has an increased anodic peak current of 4.0 to 12.6 μA and a lowered cathodic peak current of 6.1 to 2.7 μA (Fig. 7b). A decrease in redox potential ($E_{1/2}$, −0.084 V) and reversibility (ΔE_p, 168 mV) are observed after 20 minutes when the uptake of dioxygen from the environment stabilizes the one-electron Cu^{II}/Cu^{I} redox pair. The anodic peak current diminishes to 6.7 μA; however, the cathodic peak current changes slightly. A six coordinate complex-monodehydroascorbate-dioxygen adduct, [(phen)(HL^2)-Cu^{II}-(HA)(O_2)] (Fig. 7c), is formed, as shown by these observations. A one-electron Cu^{II}/Cu^{I} redox pair is consistent with a minor increase in redox potential ($E_{1/2}$, −0.076 V) and reversibility (ΔE_p, 152 mV) with no change in the cathodic peak current and an additional drop in the anodic peak current to 3.9 μA after 30 minutes. The observations are indicative of a new generation of complex-dehydroascorbatehydroperoxo species, [(phen)(HL^2)-Cu^{II}-(DA)(OOH)], (Scheme 2d). Eventually, the one-electron Cu^{II}/Cu^{I} pair (Fig. 7e) maintains

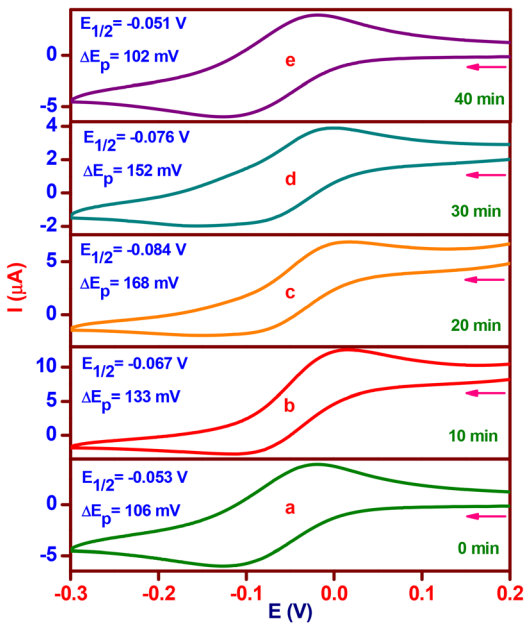

Fig. 7 Cyclic voltammetric changes of [Cu(L^2)(phen)](ClO$_4$) (**2**) upon addition of H_2A (molar ratio, 1 : 5; time interval, 10 min).

its preferential stabilization (complex **2**) with the same redox potential ($E_{1/2}$, −0.051 V), reversibility (ΔE_p, 102 mV), and cathodic and anodic peak currents (i_{pc}, 6.4; i_{pa}, 4.1 μA).

The 1 : 50 equivalent ratio of catalyst **2** and H_2A was measured using a high-resolution mass spectrum (HRMS) after mixing in methanol for 10 minutes (Fig. S28†). It shows three minor peaks at m/z = 174.08, 643.86, and 674.91 in addition to a main peak at m/z = 468.10. The former peak, which is estimated to be 469.01, corresponds to the catalyst $[Cu^{II}(L^2)(phen)]^+$. The product, DA (estimated m/z = 174.10), is indicated by the latter smaller peak at m/z = 174.08. The existence of a complex–monodehydroascorbate adduct, [(phen)(HL^2)-Cu^I-(HA)], may be responsible for another peak at m/z = 643.86 (estimated m/z = 644.23). A complex–substrate–dioxygen aggregate (estimated m/z = 675.23) containing superoxocopper(II) species (Scheme 2c) and/or hydroperoxocopper(II) species (Scheme 2d) matches with the peak at m/z = 674.91.

We have studied the catalyst–substrate reaction using UV-Vis spectroscopy, CV, and HRMS techniques in order to deduce a likely mechanism (Scheme 2) of the AOase activity of **1** and **2**. It is suggested to start with a five-coordinate Cu(I) species 'a' bonded to monodehydroascorbate, which is produced by catalyst **1** or **2**. Subsequently, it undergoes an oxidation process that converts the Cu(I) center in 'a' to a Cu(II) center in 'b' when it reacts with atmospheric oxygen. The next stage entails a crucial intramolecular proton transfer mechanism that goes through transition state 'c' to produce peroxo intermediate 'd' from the oxygen atom in the monodehydroascorbate moiety to the oxygen atom in superoxide in the 'b' intermediate.

Finally, the last step includes binding yet another molecule of the H_2A substrate to the copper center in intermediate 'd', rejuvenating the initial catalyst and releasing the expected DA product and H_2O_2. It has previously been demonstrated that the primary likely result of oxygen reduction in such catalytic cycle processes employing a Cu^{II}/Cu^I redox pair is hydrogen peroxide.[82] As a result, complexes **1** and **2** replicate the ascorbate oxidase activity of the type-2 copper sites in AOase, as demonstrated by the oxidation of H_2A with molecular oxygen to yield DA.

Oxidation of benzylamine (Ph–CH_2–NH_2) to benzaldehyde (Ph–CHO)

In a 10 mL solution of MeOH : H_2O (4 : 1 v/v) containing Ph–CH_2–NH_2 as a substrate (1×10^{-1} M), the copper(II) complex (1×10^{-3} M) using H_2O_2 (30% w/v; 1 mL) catalyzed the chemical transformation of amine into aldehyde ($RCH_2NH_2 \rightarrow RCHO + NH_3$).[80] There is no discernible Ph–CHO produced by the reaction involving Ph–CH_2–NH_2 and H_2O_2 or the complex (Fig. 8 and Fig. S29†). However, Ph–CHO production is aided by the complex-catalyzed deamination of Ph–CH_2–NH_2 in the presence of H_2O_2. Consequently, a significant yield of Ph–CHO (**1**, 0.070 g, 66%; **2**, 0.077, 72%) was produced under mild reaction conditions by effectively and selectively converting Ph–CH_2–NH_2. Ph–CHO (δ 9.83 ppm, –CHO instead of δ 3.67 ppm, –CH_2–) was observed (Fig. S30†) from ^{1}H NMR data in $CDCl_3$,

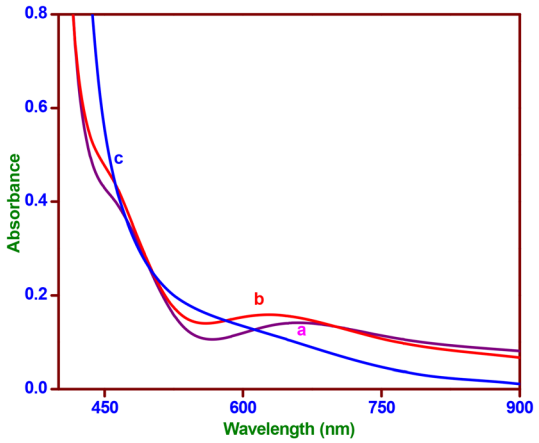

Fig. 8 Electronic spectra of $[Cu(L^2)(phen)](ClO_4)$ (**2**) in methanol : water (4 : 1 v/v) (a), addition of benzylamine to complex (b) and addition of H_2O_2 to benzylamine and complex (c).

and Ph-CHO (Fig. S31†) is associated with the substantial HRMS peak at m/z = 107.049 ($(M + H)^+$; calcd 106.120). The novel monocopper(II) complexes have therefore been developed as biomimetic catalysts that resemble AmOase to facilitate the oxidation process of an aerobic amine to an aldehyde.

The process has been monitored using UV-Vis spectrophotometry, which determines the increase in absorbance with time (60 s interval) at 252 nm to produce the Ph–CHO concentration. A room temperature aerobic reaction was carried out using both complexes (**1** or **2**: 3.3×10^{-7} M) with Ph–CH_2–NH_2 (2–12 equivalents) in an aqueous methanolic solution containing H_2O_2 (50 equivalents) (Fig. S32†). The kinetic features of the reaction have been explored through the use of the function of the initial rate process. The Michaelis–Menten approach was applied to assess the measured rate *vs.* concentration of the substrate. The linearization was performed using the Lineweaver–Burk plot, which produced the maximal initial rate, V_{max} [43.4 (**1**) or 50.4×10^{-4} Ms^{-1} (**2**)], and Michaelis–Menten constant, K_M [38.1 (**1**) or 39.5×10^{-4} M (**2**)]. The computation of the turnover number, k_{cat} [4.7 (**1**) or 5.4×10^5 h^{-1} (**2**)] (Fig. S33 and S34†), involved dividing the maximal initial rate by the concentration of the related complexes. The outcomes demonstrate the significant efficacy of both complexes towards the oxidation of Ph–CH_2–NH_2. As expected, there is more activity in **2** than in **1**. The phenolate oxygen donor of the Schiff base is readily dissociable, and the coordination number surrounding copper(II) is smaller. It is possible that these properties, which facilitate substrate attachment to the metal center, account for the high reactivity of the complexes.

The catalytic oxidation of Ph–CH_2–NH_2 with copper(II) complexes as catalysts was suggested as a potential mechanism (Scheme 3). First, a six-coordinate adduct between the copper(II) complex and benzylamine is formed, denoted as $[Cu^{II}(L^n)(phen)(C_6H_5\text{-}CH_2\text{-}NH_2)]^+$ (A), which has an octahedral geometry and a $Cu^{II}N_5O$ chromophore; (a) electronic spectra showed that an adduct formed and the visible band changed from 684 to 680 nm (**1**) and 670 to 628 nm (**2**) (hypsochromic shift); (b)

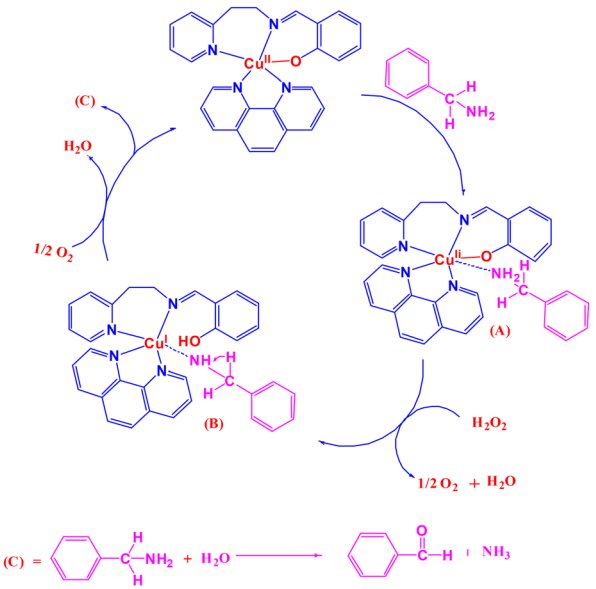

Scheme 3 Based on the findings of the experiment, a catalytic cycle for the oxidation of Ph–CH_2–NH_2 to Ph–CHO, {catalyst, [Cu(L^2)(phen)] ClO_4 (**2**)}.

electrochemical measurements demonstrated that the redox potential ($E_{1/2}$) (Fig. 9 and Fig. S35†) moved to a more negative value (**1**, 0.044 to −0.029; **2**, 0.035 to −0.037 V); and mass spectra (Fig. S36†) revealed that the HRMS peak emerged at *m*/*z*, 575.40 (calc. 575.71) (**2**). The second stage was the reaction of the adduct with H_2O_2 to cause a color change from green to brown, resulting in the vanishing of the d–d band. In parallel, the chromophore transitioned from $Cu^{II}N_5O$ (Cu^{II}-adduct, A) to $Cu^{I}N_5$ (Cu^{I}-adduct, B), whereby Cu(II) underwent reduction to Cu(I). In the third stage, B undergoes five simultaneous changes: (i) the Cu(I) oxidized to Cu(II) by molecular oxygen,(II) the O_2 reduced to H_2O, (iii) the C(α)–H bond ruptured, (iv) a hydride ion is transferred from the methylene group, and (v) the benzylimine (C_6H_5–CH═NH) intermediate is discharged; and the catalyst, $[Cu(L^n)(phen)]^+$, is regenerated. Lastly, in the presence of water, C_6H_5–CH═NH underwent further hydrolysis to produce Ph–CHO and NH_3.[83] The oxidation of amine to aldehyde with molecular oxygen is catalyzed by complexes **1** and **2**, which are similar to an enzymatic reaction[84] of the type-2 copper core in AmOase.

Oxidation of 3,5-di-*tert*-butylcatechol (3,5-DTBC) to 3,5-di-*tert*-butylquinone (3,5-DTBQ)

The potential of copper(II) complexes to function as functional models of catechol oxidase was assessed by using them as catalysts in the oxidation of 3,5-di-*tert*-butylcatechol (3,5-DTBC) to 3,5-di-*tert*-butylquinone (3,5-DTBQ). Both monocopper(II) complexes exhibit comparable behavior in methanol solution (MS) and buffer solution (BS) at optimal pH (Fig. S37 and S38†) and the representative spectral change for **2** is displayed in Fig. 10 and Fig. S39–S41.† In order to investigate the catalytic activity of **1** or **2**, 1.45×10^{-3} M of 3,5-DTBC was added to 2.9×10^{-5} M (MS) or 2.9×10^{-6} M (BS) complex solutions [catalyst : substrate ratio, 1 : 50 (MS) or 1 : 500 (BS)]. Following the addition of 3,5-DTBC to catalyst **1** or **2**, the reaction was observed for 3 h (MS) or 30 min (BS). In the beginning, both complexes exhibit bands in MS at 400 (**1**) or 390 (**2**) nm and in BS at 404 (**1**) or 399 (**2**) nm. The spectral run completed in the time limit shows an increase in absorbance almost above that band upon the addition of 3,5-DTBC. The experiment clearly demonstrates the oxidation of 3,5-DTBC to 3,5-DTBQ, which is accelerated by the monocopper(II) complexes. This is because it is commonly known that in MS or BS, 3,5-DTBQ displays band maxima in the 390–404 nm range. Even so, when the autoxidation of 3,5-DTBC alone was examined in both media (MS and BS), it seemed that this process was either weak or nonexistent (Fig. S42 and S43†).

3,5-DTBQ was purified by column chromatography using a 10% ethyl acetate and hexane solution as the eluent. It was then extracted from the reaction mixture in MS with a significant yield (**1**, 70.7; **2**, 71.2%). By measuring its melting point

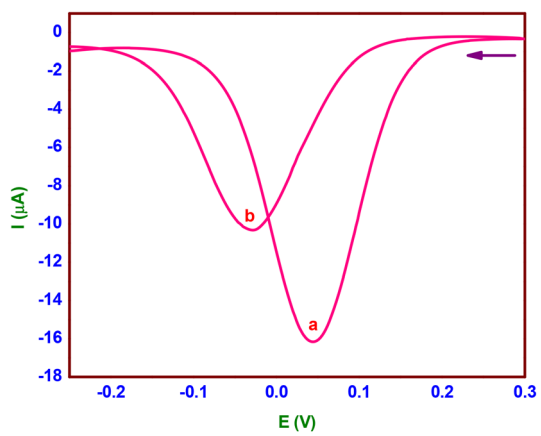

Fig. 9 Differential pulse voltammogram of $[Cu(L^2)(phen)]^+$ **2** (a) and the adduct formed by the addition of benzylamine (molar ratio, 1 : 10) (b).

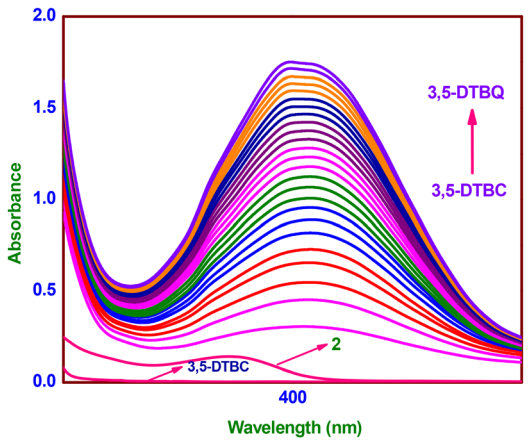

Fig. 10 Oxidation of 3,5-DTBC by the catalyst [Cu(L^2)(phen)](ClO_4) (**2**) in buffer solution (pH 7.8) monitored by UV-Vis spectroscopy.

(**1**, 109; **2**, 111 °C; and literature value, 110 °C),[85] FTIR (Fig. S44†) in KBr (**2**: $\tilde{\nu}$(O–H) bands absent at 3460 and 3260 cm^{-1}; the $\tilde{\nu}$(C=O) band present at 1657 cm^{-1}) and ^{1}H NMR (Fig. S45†) in $CDCl_3$ [**2**: $-CH_3$ (C), s, δ 1.16 ppm, 9H; $-CH_3$ (D), s, δ 1.20 ppm, 9H; H (B), s, δ 6.15 ppm, 1H; H (A), s, δ 6.87 ppm, 1H], the isolated 3,5-DTBQ was identified.

The rate constant for a catalyst complex was found using the conventional initial rate method in order to comprehend the kinetic component of catalysis for **1** or **2**. Following that, the observed rates *versus* substrate concentration data were examined using the Michaelis–Menten method of enzyme kinetics. The maximum initial rate (V_{max}) [MS, 20.2 (**1**) or 8.4 × 10^{-4} M min^{-1} (**2**); BS, 12.1 (**1**) or 14.0 × 10^{-4} M s^{-1} (**2**)], and the Michaelis–Menten constant, (K_M) [MS, 1.2 (**1**) or 0.4 × 10^{-4} M (**2**); BS, 12.0 (**1**) or 16.9 × 10^{-4} M (**2**)], were found by linearization utilizing Lineweaver–Burk plots (Fig. 11 and Fig. S46–S50†).[86] By dividing the V_{max} values by the concentration of the respective complexes, the turnover number (k_{cat}) [MS, 2.6 (**1**) or 1.7 × 10^3 h^{-1} (**2**); BS, 1.5 (**1**) or 1.7 × 10^6 h^{-1} (**2**)] values were determined. The data clearly show that both complexes **1** and **2** are quite active. The phenolate oxygen atom in complex **1** or **2** is labile, which may facilitate the catalyst–substrate interaction by forming a positive channel. This may be a necessary condition for exhibiting higher catalytic activities, which could explain the unusually high activity of the monocopper(II) complexes. The catalyst–substrate complex in BS is substantially more stable than in MS at optimum pH, as shown by the K_M value in BS being 10 (**1**) or 42 (**2**) times more than that of MS. Additionally, the complexes exhibit a greater turnover number in BS at the optimum pH, while the turnover number in MS exhibits the opposite effect. It is approximately 577 (**1**) or 1000 (**2**) times greater in BS than in MS. In this instance, complex **2** performs better than complex **1**, demonstrating higher catecholase activity.

Based on the differences in activities, it appears that the lability of coordinated phenolate oxygen is easier in the equatorial position and that substrate substitution occurs more quickly in **2** than in **1**. The flexible 665 chelate rings in **2** instead of the rigid 655 chelate rings in **1** cause high structural distortion. This enables easy access to the substrate, maximizing the steric match between the complex and the substrate, which promotes a more efficient inner-sphere electron transfer process that elevates catalytic activity.

The aerobic interaction between 100 equivalents of 3,5-DTBC and the complex (**1** or **2**, 3.3 × 10^{-3} M) in MS (Fig. 12 and Fig. S49†) was investigated using UV-Visible spectroscopy. The complex oxidizes 3,5-DTBC and converts 3,5-DTBQ, which results in the loss of the d–d band (Fig. 12b and Fig. S49b†) at 678 nm (**1**) or 670 nm (**2**) due to the Cu(II) to Cu(I) reduction produced by the addition of 3,5-DTBC and a rise in absorbance (Fig. 12d and Fig. S49d†) at 396 nm (**1**) or 398 nm (**2**). Following the completion of the reaction, the uptake of molecular oxygen by the solution displayed another significant absorbance peak (Fig. 12c and Fig. S49d†) at either 557 nm (**1**) or 571 nm (**2**). This was most probably the result of the superoxide (O_2^-)-to-Cu(II) LMCT transition, which suggested the formation of a superoxocopper(II) intermediate.[87]

Conversely, differential pulse voltammetry (DPV) was used to study both the complex (**1** or **2**, 0.001 M) and 3,5-DTBC (molar ratio 1 : 5) in MS at intervals of five minutes throughout the reaction (Fig. 13 and Fig. S50†). When 3,5-DTBC is added to the complex solution, two peaks appear at two distinct $E_{1/2}$, representing Cu^{II}/Cu^{I} and Cu^{I}/Cu^{II} one-electron redox pairs (Fig. 13b and Fig. S46b†) at +0.015 V (*i*, 15.9 μA) and +0.055 V (*i*, 15.7 μA) (**1**) or −0.027 V (*i*, 18.7 μA) and +0.054 V (*i*, 16.9 μA) (**2**), respectively. This suggests the formation of a copper(II) adduct bound to monocatecholate, which is then reduced right away to produce copper(I) species bound to monocatecholate (quick, Scheme 4b). The peak (**1**: $E_{1/2}$, + 0.055 V; *i*, 15.7 μA or **2**: $E_{1/2}$, + 0.054 V; *i*, 16.9 μA) shifted to −87 mV (**1**) or −79 mV (**2**) after 10 min (Fig. 13c and Fig. S46c†), showing a one-electron Cu^{II}/Cu^{I} redox pair. Reduction becomes challenging due to the conversion of molecular oxygen bonding to copper(I) species bound to monocatecholate, as evidenced by a

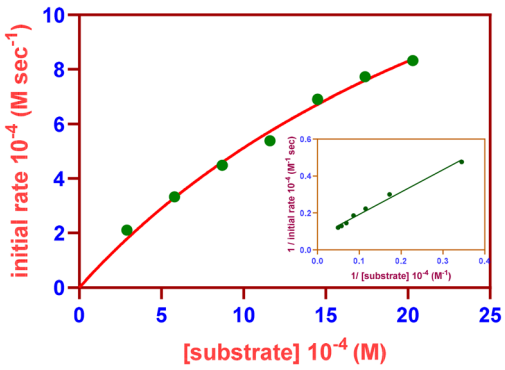

Fig. 11 Reaction rate for the oxidation reaction catalyzed by [Cu(L^2)(phen)](ClO_4) (**2**) depending on the concentration of 3,5-DTBC in buffer solution (pH 7.8). Inset: Lineweaver–Burk plot.

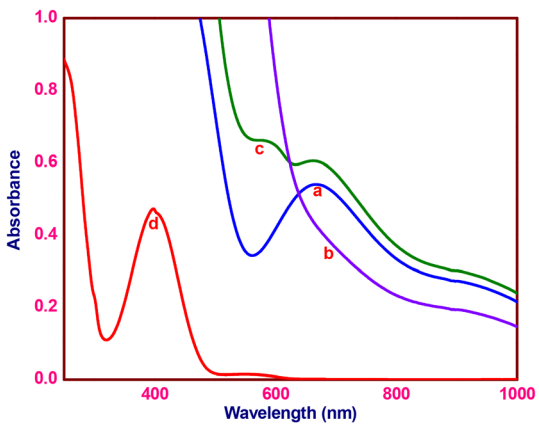

Fig. 12 Electronic spectral changes of [Cu(L^2)(phen)](ClO_4) (**2**) (3.3 × 10^{-3} M) upon addition of 3,5-DTBC (molar ratio, 1 : 100) in MeOH. The electronic spectrum of complex (a), disappearance of the d–d band immediately after the addition of 3,5-DTBC (b), formation of a superoxide intermediate (c) and generation of 3,5-DTBQ (d).

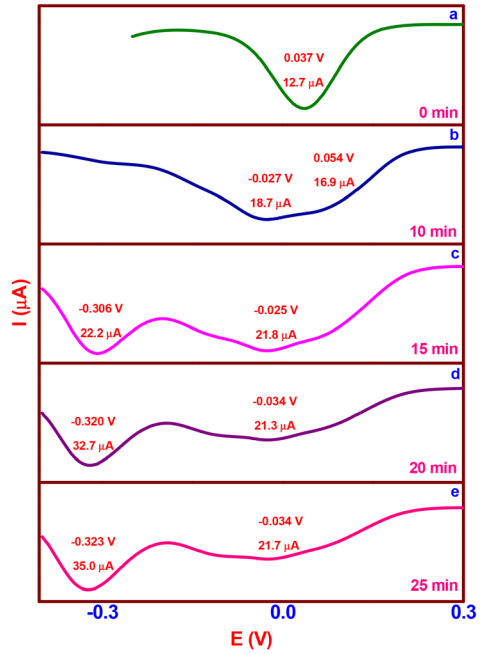

Fig. 13 Differential pulse voltammetric changes of [Cu(L^2)(phen)](ClO_4) (**2**) upon addition of 3,5-DTBC (molar ratio, 1 : 5; time interval, 5 min).

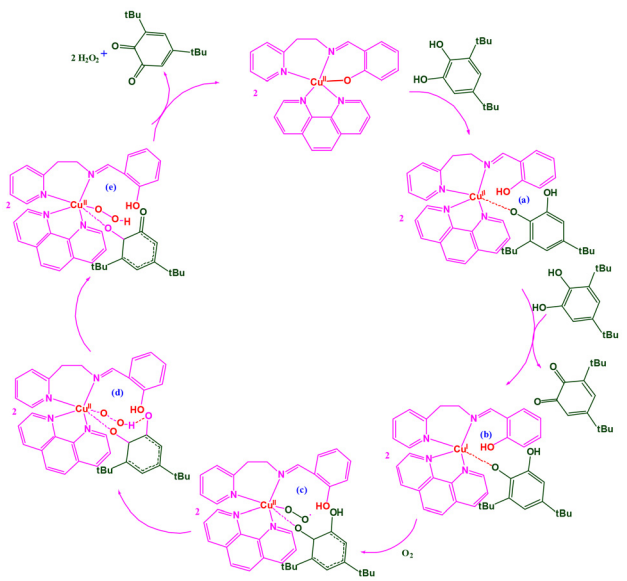

Scheme 4 Based on observations from experiments, a plausible catalytic cycle for the oxidation of 3,5-DTBC to 3,5-DTBQ {catalyst, [Cu(L^2)(phen)]ClO_4 (**2**)}.

rise in electron density on Cu(II) and an opposite trend in $E_{1/2}$. This has something to do with the development of the superoxocopper(II) intermediate (Scheme 4c). Additionally, the DPV displays a peak (Fig. 13c–13e and Fig. S46c to 46e†) at an $E_{1/2}$ value of −0.308 to −0.319 V (*i*, 19.8–34.8 μA) (**1**) or −0.306 to −0.323 V (*i*, 22.2–35.0 μA) (**2**). Furthermore, an increase in current is observed (*i*: **1**, 15.0; **2**, 13.8 μA), consistent with the formation of hydroperoxocopper(II) species (Scheme 4e).

HRMS measurements were taken in MS (Fig. S51 and S52†) and BS (Fig. S53 and S54†) after reacting the complex (**1** or **2**) with 3,5-DTBC (molar ratio 1 : 50) and allowing it to react for 10 minutes. The most common species is produced from the monomer $[Cu^{II}(L^1)(phen)]^+$ (**1**) or $[Cu^{II}(L^2)(phen)]^+$ (**2**) at *m*/*z* = 454.16 (MS)/454.23 (BS) (**1**) or 468.15 (MS)/468.12 (BS) (**2**). It is possible that a monocatecholate-bound copper(II) or monocatecholate-bound copper(I) adduct exists as a prominent peak at *m*/*z* = 676.77 (MS)/676.61 (BS) (calculated 676.89) (**1**) or 690.13 (MS)/690.47 (BS) (calculated 690.75) (**2**). According to Scheme 4a and b, they can be understood as either $[(phen)(HL^1/HL^2)Cu^{II}\text{-}(3,5\text{-}DTBC^{1-})]^+$ or $[(phen)(HL^1/HL^2)Cu^{I}\text{-}(3,5\text{-}DTBC^{1-})]$. At *m*/*z* = 243.19 (MS)/243.15 (BS) (calculated 243.29) (**1**) or 243.16 (MS)/243.12 (BS) (calculated 243.29) (**2**), a well-defined peak for the product 3,5-DTBQ and Na^+ was found. The complex–substrate–dioxygen aggregate is specifically responsible for the peak at *m*/*z* = 708.55 (MS)/708.46 (BS) (calculated 708.88) (**1**) or 722.15 (MS)/722.89 (BS) (calculated 722.97) (**2**). This is appropriate with the creation of intermediates, either superoxocopper(II), $[(phen)(HL^1/HL^2)\text{-}Cu^{II}\text{-}(3,5\text{-}DTBC^{1-})(O_2^{-})]$ (Scheme 4c), or hydroperoxocopper(II), $[(phen)(HL^1/HL^2)\text{-}Cu^{II}\text{-}(3,5\text{-}DTBQ^{1-})(HOO^{-})]$ (Scheme 4e).

At ambient temperature, the reactivity of [Cu(L^1)(phen)](ClO_4) (**1**) or [Cu(L^2)(phen)](ClO_4) (**2**) with H_2O_2 was observed using UV-Vis spectroscopy in CH_3CN (Fig. S55 and S56†). It can be observed from the results that the complex is evolving into a new species with an absorption band at λ_{max} = 370 (**1**) or 368 nm (**2**).[27] The absorption band enables an LMCT from the hydroperoxide ligand to the Cu(II) ion. These findings imply that $[Cu^{II}(L^1/L^2)(phen)]^+$ transforms into $[Cu^{II}(HL^1/HL^2)(phen)(OOH)]^+$. The hydroperoxocopper(II) complex develops slowly at room temperature, and it requires an hour for the resultant species to stabilize. Also, we must ascertain in the event, dioxygen undergoes reduction to H_2O_2 or water throughout the oxidation (H_2A or 3,5-DTBC) process. A thorough work-up of the mixture of H_2A or 3,5-DTBC, complex **2**, and KI clearly indicates that dioxygen is reduced to H_2O_2, as reported by other investigators as well.[88] This is supported by the oxidation of I^- to I_2 and subsequent production of I_3^-, as shown by the UV-visible spectral study of the solution (Fig. S57†). Notably, superoxide is the starting point for the formation of H_2O_2. Moreover, the results provided evidence for the production of the hydroperoxocopper(II) intermediate and the subsequent emergence of H_2O_2 during the catalytic cycle of oxidation of different substrates like H_2A or 3,5-DTBC.

As a result, the following is a description of Scheme 4, which represents the most likely catalytic mechanism. In the beginning, the catalyst and 3,5-DTBC react to produce monocatecholate-bound copper(II) species (a). Following that, the copper(II) species (a) undergo fast reduction to a monocatecholate-bound copper(I) species (fast, b). Subsequently, the copper (I) center in (b) is then oxidized to a copper(II) center with aerial oxygen, resulting in the superoxocopper(II) intermediate (c). Afterwards, a proton is transferred from the unbound catecholate oxygen atom (c) to the superoxide bound to copper(II) (d) in the rate-determining step, which generates hydroperoxo-

copper(II) species (e). In the end, when 3,5-DTBQ is discharged from (e), H_2O_2 is released, returning the catalyst to its initial active state. According to the outcomes, copper(II) is reduced to copper(I) and there is a monocatecholate-bound copper(I) adduct; these events come together to form complex–substrate–dioxygen intermediates that catalytically convert catechol to *o*-quinone in order to resemble the functions of type-3 COase.

One benefit of the current model systems over the original enzyme is their capacity to perform in methanol solution. When comparing the values of mono- and dicopper(II) complexes in the literature, the turnover number of **1** or **2** is divided into three categories: (a) greater (3–943 h^{-1}),[89,90] (b) comparable (1.38–9.11 × 10^3 h^{-1})[91,92] and (c) smaller (1.09 × 10^4–1.09 × 10^5 h^{-1}).[93,94] The complexes in buffer solution [1.5 × 10^6 h^{-1} (**1**) or 1.7 × 10^6 h^{-1} (**2**)], on the other hand, exhibit a turnover number 2.3–2.6 times smaller than the value for the dinuclear copper(II) complex, $[Cu_2L(NO_3)_2]$ (H_2L = *N*,*N*′-bis(3-methoxysalicylidene)-1,3-propanediamine), reported by Terán *et al.* (3.89 × 10^6 h^{-1}).[95] It is one of the most potent catalytic models and is closer in value to the COase enzyme that was isolated from *Ipomoea batatas* (8.25 × 10^6 h^{-1}).[96] Interestingly, the new complexes displayed greater turnover numbers than the COase enzyme isolated from *Lycopus europaeus* (5.7 × 10^5 h^{-1}).[97] Considering that the Cu^{II}/Cu^{I} redox potential is crucial to the oxidation of catechol, both complexes work as efficient catalysts in MS and BS to convert 3,5-DTBC into 3,5-DTBQ.[98] A basic limitation of the model complexes (mono- and dinuclear) is that most mimics show relatively modest catalytic activity in comparison with the enzymes. This means that there are always rooms for improvement in the design of structural and functional model systems that are more industrially potential and closely aligned with the enzyme attributable to the structure–property relationship. It follows that the monocopper(II) complex **1** or **2** is the most effective catalyst model for this oxidation process, and that the turnover number value is the highest that has been reported, complementing the quality of the enzyme assay of catechol oxidase.

Conclusions

Novel monocopper(II) complexes with mixed-ligands (tridentate NNO and bidentate NN donors) have been synthesized. The geometry of the complex ion among the active model complexes shows a distorted (3 + 2) trigonal bipyramidal (NNO + NN), which surrounds copper(II) and corresponds to the CuN_4O chromophore. An attractive C–H···π and the inter-pair π···π non-covalent interactions lead to the construction of dimers, as indicated by crystal packing. Using DFT, structural optimization and electronic parameter calculations were carried out to comprehend the chemical reactivity, stability, and selectivity of both complexes in solution. The optimized structures show that the coordination geometry of the copper center is distorted square pyramidal. The solid-state electronic absorption spectra illustrate a broad band, whereas the polycrystalline EPR spectra show a considerable shift toward the trigonal bipyramidal ($g_\perp > g_\parallel$; $g_\parallel \approx g_e$) geometry in addition to the axial symmetry. However, in a solution, they lean toward the axially symmetric, distorted square pyramidal shape characteristics of monocopper(II) five-coordinate complexes. The structural distortion of the positive Cu^{II}/Cu^{I} redox couple facilitates simple interconversion between Cu^{I} and Cu^{II} redox states and makes the pair chemically and electrochemically reversible. This is because the appropriate chelate ring sizes of the models provide the coordination mode with a minimal amount of stereochemical reorganization while preserving the stability of the Cu^{I} and Cu^{II} states.

Biomimetic catalytic oxidative reactions can be effectively imitated by the monocopper(II) complexes. It emerged that both catalysts in **MS** and/or **BS** favored three different chemical transformations under benign conditions and functioning as a single active site, specifically, $H_2A \rightarrow DA$ [k_{cat}: AOase, **MS**, 4.8 (**1**) or 8.5 × 10^6 h^{-1} (**2**); **BS**, 2.5 (**1**) or 5.2 × 10^7 h^{-1} (**2**)], Ph–CH_2–NH_2 → Ph-CHO [k_{cat}: AmOase, 4.7 (**1**) or 5.4 × 10^5 h^{-1} (**2**)], and 3,5-DTBC → 3,5-DTBQ [k_{cat}: COase, **MS**, 2.6 (**1**) or 1.7 × 10^3 h^{-1} (**2**); **BS**, 1.5 (**1**) or 1.7 × 10^6 h^{-1} (**2**)]. Based on their k_{cat} values, they demonstrate a high degree of AmOase activity. The k_{cat} values for their activities in buffer solution are more similar to the turnover number of natural enzymes (AOase, 2.45 × 10^6 h^{-1} and 3.1 × 10^7 h^{-1}; COase, 5.7 × 10^5 h^{-1} and 8.25 × 10^6 h^{-1}). Interestingly, for these catalytic processes, these values represent the highest turnover number for monocopper (II) complexes that has been reported to date.

In summary, several characteristics, such as the labile coordinated oxygen donor, the appropriate chelate ring size, the flexibility of the coordinated planar phen, structural distortion, the ease of the substrate–catalyst association, and the positive (Cu^{II}/Cu^{I}) redox potential, can be attributed to the higher activity of catalysts for enzyme (AOase, AmOase, and COase) modeling catalysis. As a result, both monocopper(II) complexes exhibit the features of the most potent promiscuous catalysts, making them suitable models for oxidation processes and amplify the activity of copper oxidase enzymes. The comprehension of the three probable mechanistic routes has been enhanced by the catalytic promiscuity of the functional biomimetics. Gaining an understanding of functional biomimetics allows one to catalyze a number of important and industrially relevant organic syntheses

Author contributions

Vigneswara Chellam Ravisankar: formal analysis, investigation, and methodology; Balasubramaniam Selvakumaran: data curation, formal analysis, investigation, methodology, and writing – original draft; Tamilarasan Ajaykamal: methodology and software; Mariappan Murali: conceptualization, funding acquisition, investigation, methodology, project administration, resources, supervision, writing – original draft, and writing – review and editing.

Data availability

The data supporting this article have been included as part of the ESI.†

Conflicts of interest

There are no conflicts to declare.

Acknowledgements

The authors are thankful to the ANRF-Science and Engineering Research Board (SERB), India, for the financial support (CRG/2022/002225 and EMR/2016/007756). The authors further thank Professor R. Murugavel, Indian Institute of Technology Bombay, Mumbai, for providing them access to single crystal X-ray diffraction testing that was made possible by an excellent investigator award from the DAE-SRC. We express our gratitude to the Sophisticated Analytical Instrumentation Facility (SAIF), Indian Institute of Technology Madras, Chennai for providing the EPR facility. BS is grateful to the Tamil Nadu State Council for Science and Technology (TNSCST), Chennai, for the RFRS fellowship (TNSCST/RFRS/08/VM/2021-22).

References

1 S. V. Ley, *Comprehensive Organic Synthesis: Selectivity, Strategy and Efficiency in Modern Organic Chemistry*, Oxidation, 1992, vol. 7.
2 R. A. Sheldon and J. K. Kochi, *Metal-Catalyzed Oxidations of Organic Compounds*, 1981.
3 B. Cornils, in *Green Chemistry and Catalysis*, ed. R. A. Sheldon, I. Arends and U. Hanefeld, 2007.
4 C. S. Foote, J. S. Valentine, A. Greenberg and J. F. Liebman, Active Oxygen in Chemistry, in *Struct. Energ. React. Chem. Ser*, 1995, vol. 2.
5 M. Rolff, J. Schottenheim, H. Decker and F. Tuczek, *Chem. Soc. Rev.*, 2011, **40**, 4077–4098.
6 E. I. Solomon, R. Sarangi, J. S. Woertink, A. J. Augustine, J. Yoon and S. Ghosh, *Acc. Chem. Res.*, 2007, **40**, 581–591.
7 S. Friedle, E. Reisner and S. J. Lippard, *Chem. Soc. Rev.*, 2010, **39**, 2768–2779.
8 L. Que Jr and W. B. Tolman, *Nature*, 2008, **455**, 333–340.
9 T. Punniyamurthy, S. Velusamy and J. Iqbal, *Chem. Rev.*, 2005, **105**, 2329–2364.
10 E. I. Solomon, D. E. Heppner, E. M. Johnston, J. W. Ginsbach, J. Cirera, M. Qayyum, M. T. K. Emmons, C. H. Kjaergaard, R. Hadt and L. Tian, *Chem. Rev.*, 2014, **114**, 3659–3853.
11 H. Pracejus, *Adv. Synth. Catal.*, 1975, **317**, 350–351.
12 L. Casella, E. Monzani, L. Santagostini, L. D. Gioia, M. Gullotti, P. Fantucci, T. Beringhelli and A. Marchesini, *Coord. Chem. Rev.*, 1999, **185**, 619–628.
13 A. Messerschmidt, A. Rossi, R. Ladenstein, R. Huber, M. Bolognesi, G. Gatti, A. Machesini, R. Petruzzelli and A. Finazzi-Agró, *J. Mol. Biol.*, 1989, **206**, 513–529.
14 A. Messerschmidt, R. Ladenstein and R. Huber, *J. Mol. Biol.*, 1993, **230**, 997–1014.
15 A. L. Hughes, *Immunogenetics*, 1999, **49**, 106–114.
16 T. Klabunde, C. Eicken, J. C. Sacchettini and B. Krebs, *Nat. Struct. Biol.*, 1998, **5**, 1084–1090.
17 C. Gerdemann, C. Eicken and B. Krebs, *Acc. Chem. Res.*, 2002, **35**, 183–191.
18 E. I. Solomon, U. M. Sundaram and T. E. Machonkin, *Chem. Rev.*, 1996, **96**, 2563–2606.
19 I. A. Koval, P. Gamez, C. Belle, K. Selmeczi and J. Reedijk, *Chem. Soc. Rev.*, 2006, **35**, 814–840.
20 B. J. Deverall, *Nature*, 1961, **189**, 311.
21 M. Zhao, H. B. Eang, L. N. Ji and Z. W. Mao, *Chem. Soc. Rev.*, 2013, **42**, 8360–8375.
22 M. Guell and P. E. M. Siegbahn, *J. Biol. Inorg. Chem.*, 2007, **12**, 1251–1264.
23 B. T. O. Holt, M. A. Vance, L. M. Mirica, D. E. Heppner, T. D. P. Stack and E. I. Solomon, *J. Am. Chem. Soc.*, 2009, **131**, 6421–6438.
24 S. K. Dey and A. Mukherjee, *Coord. Chem. Rev.*, 2016, **310**, 80–115.
25 A. Biswas, L. K. Das, M. G. B. Drew, C. Diaz and A. Ghosh, *Inorg. Chem.*, 2012, **51**, 10111–10121.
26 K. Hult and P. Berglund, *Trends Biotechnol.*, 2007, **25**, 231–238.
27 T. P. Camargo, F. F. Maia, C. Chaves, B. D. Souza, A. J. Bortoluzzi, N. Castilho, T. Bortolotto, H. Terenzi, E. E. Castellano, W. Haase, Z. Tomkowicz, R. A. Peralta and A. Neves, *J. Inorg. Biochem.*, 2015, **146**, 77–88.
28 A. Altomare, G. Cascarano, C. Giacovazzo and A. Guagliardi, *J. Appl. Crystallogr.*, 1993, **26**, 343–350.
29 G. M. Sheldrick, *Acta Crystallogr., Sect. C:Struct. Chem.*, 2015, **C71**, 3–8.
30 L. J. Farrugia, *J. Appl. Crystallogr.*, 2012, **45**, 849–854.
31 B. Selvakumaran, M. Murali, S. Shanmugavadivel and S. Sindhuja, *J. Inorg. Biochem.*, 2024, **259**, 112671.
32 D. Jiang, X. Li, L. Liu, G. B. Yagnik and F. Zhou, *J. Phys. Chem. B*, 2010, **114**, 4896–4903.
33 P. A. N. Reddy, M. Nethaji and A. R. Chakravarty, *Inorg. Chim. Acta*, 2002, **337**, 450–458.
34 A. K. Ghosh, A. Ali, Y. Singh, C. S. Purohit and R. Ghosh, *Inorg. Chim. Acta*, 2018, **474**, 156–163.
35 A. Santra, G. Mondal, M. Acharjya, P. Bera, A. Panja, T. K. Mandal, P. Mitra and P. Bera, *Polyhedron*, 2016, **113**, 5–15.
36 S. Mondal, M. Chakraborty, A. Mondal, B. Pakhira, A. J. Blake, E. Sinn and S. K. Chattopadhyay, *New J. Chem.*, 2018, **42**, 9588–9597.
37 W. J. Geary, *Coord. Chem. Rev.*, 1971, **7**, 81–122.
38 V. Sathya and M. Murali, *Inorg. Chem. Commun.*, 2018, **92**, 55–59.
39 J. B. Bates, L. M. Toth, A. S. Quist and G. E. Boyd, *Spectrochim. Acta, Part A*, 1973, **29**, 1585–1600.

40 S. Sangeetha, T. Ajaykamal and M. Murali, *New J. Chem.*, 2021, **45**, 7578–7593.
41 I. C. Mendes, J. P. Moreira, A. S. Mangrich, S. P. Balena, B. L. Rodrigues and H. Beraldo, *Polyhedron*, 2007, **26**, 3263–3270.
42 E. Montiel, A. J. Cruz, N. Jayanthi, S. Bernés and T. Pandiyan, *Aust. J. Chem.*, 2010, **63**, 965–977.
43 G. A. V. Albada, A. Mohamadou, I. Mutikainen, U. Turpeinen and J. Reedijk, *Eur. J. Inorg. Chem.*, 2004, 3733–3742.
44 A. W. Addison, T. N. Rao, J. Reedijk, J. van Rijn and G. C. Verschoor, *J. Chem. Soc., Dalton Trans.*, 1984, 1349–1356.
45 K. Gudasi, R. Vadavi, R. Shenoy, M. Patil, S. A. Patil and M. Nethaji, *Inorg. Chim. Acta*, 2005, **358**, 3799–3806.
46 J. L. Viegas and S. N. Dhuri, *J. Mol. Struct.*, 2023, **1288**, 135719.
47 M. Egli and S. Sarkhel, *Acc. Chem. Res.*, 2007, **40**, 197–205.
48 T. J. Mooibroek, P. Gamez and J. Reedijk, *CrystEngComm*, 2008, **10**, 1501–1515.
49 P. Chakraborty, S. Purkait, S. Mondal, A. Bauzá, A. Frontera, C. Masserac and D. Das, *CrystEngComm*, 2015, **17**, 4680–4690.
50 T. H. Huang, H. Yang, G. Yang, S. L. Zhu and C. L. Zhang, *Inorg. Chim. Acta*, 2017, **455**, 1–8.
51 M. J. Frisch, G. W. Trucks, H. B. Schlegel, G. E. Scuseria, M. A. Robb, J. R. Cheeseman, G. Scalmani, V. Barone, B. Mennucci, G. A. Petersson, H. Nakatsuji, M. Caricato, X. Li, H. P. Hratchian, A. F. Izmaylov, J. Bloino, G. Zheng, J. L. Sonnenberg, M. Hada, M. Ehara, K. Toyota, R. Fukuda, J. Hasegawa, M. Ishida, T. Nakajima, Y. Honda, O. Kitao, H. Nakai, T. Vreven, J. A. Montgomery Jr, J. E. Peralta, F. Ogliaro, M. Bearpark, J. J. Heyd, E. Brothers, K. N. Kudin, V. N. Staroverov, R. Kobayashi, J. Normand, K. Raghavachari, A. Rendell, J. C. Burant, S. S. Iyengar, J. Tomasi, M. Cossi, N. Rega, J. M. Millam, M. Klene, J. E. Knox, J. B. Cross, V. Bakken, C. Adamo, J. Jaramillo, R. Gomperts, R. E. Stratmann, O. Yazyev, A. J. Austin, R. Cammi, C. Pomelli, J. W. Ochterski, R. L. Martin, K. Morokuma, V. G. Zakrzewski, G. A. Voth, P. Salvador, J. J. Dannenberg, S. Dapprich, A. D. Daniels, O. Farkas, J. B. Foresman, J. V. Ortiz, J. Cioslowski and D. J. Fox, *Gaussian 09 (Revision D.01)*, Gaussian Inc., Wallingford, CT, 2009.
52 N. Cankaya, E. Tanıs, H. E. Gülbas and N. Bulut, *Polym. Bull.*, 2019, **76**, 3297–3327.
53 C.-G. Zhan, J. A. Nichols and D. A. Dixon, *J. Phys. Chem. A*, 2003, **107**, 4184–4195.
54 J. D. Bradley and G. C. Gerrans, *J. Chem. Educ.*, 1973, **50**, 463–466.
55 W. T. Yang and R. G. Parr, *Proc. Natl. Acad. Sci. U. S. A.*, 1985, **82**, 6723–6726.
56 M. Berkowitz, *J. Am. Chem. Soc.*, 1987, **109**, 4823–4825.
57 S. B. Liu, *J. Chem. Sci.*, 2006, **117**, 477–483.
58 L. Shen, H. Y. Zhang and H. F. Ji, *J. Mol. Struct.: THEOCHEM*, 2007, **817**, 161–162.
59 M. M. Lawal, T. Govender, G. E. Maguire, H. G. Kruger and B. Honarparvar, *Int. J. Quantum Chem.*, 2018, **118**, e25497.
60 I. M. Procter, B. J. Hathaway, D. E. Billing, R. Dudley and P. Nicholls, *J. Chem. Soc. A*, 1969, 1192–1197.
61 D. E. Billing, R. Dudley, B. J. Hathaway and A. A. G. Tomlinson, *J. Chem. Soc. A*, 1971, 691–696.
62 W. Fitzgerald and B. J. Hathaway, *J. Chem. Soc., Dalton Trans.*, 1981, 567–574.
63 B. J. Hathaway and D. E. Billing, *Coord. Chem. Rev.*, 1970, **5**, 143–207.
64 A. B. P. Lever, *Inorganic Electronic Spectroscopy*, Elsevier, Amsterdam, 1970.
65 E. Garribba and G. Micera, *J. Chem. Educ.*, 2006, **83**, 1229–1232.
66 Z. Lu, C. Duan, Y. Tian, X. You and X. Huang, *Inorg. Chem.*, 1996, **35**, 2253–2258.
67 A. M. Fathy, M. M. Hessien, M. M. Ibrahim and A. E. M. M. Ramadan, *J. Mol. Struct.*, 2022, **1250**, 131809.
68 P. S. Subramanian, E. Suresh, P. Dastidar, S. Waghmode and D. Srinivas, *Inorg. Chem.*, 2001, **40**, 4291–4301.
69 D. Kivelson and R. Neiman, *J. Chem. Phys.*, 1961, **35**, 149–155.
70 S. D. Sid, O. B. Baitich and J. P. Deloume, *Polyhedron*, 1997, **16**, 2175–2182.
71 A. W. Addison, M. Carpenter, L. M. K. Lau and M. Wicholas, *Inorg. Chem.*, 1978, **17**, 1545–1552.
72 P. Tamil Selvi, M. Murali, M. Palaniandavar, M. Kockerling and G. Henkel, *Inorg. Chim. Acta*, 2002, **340**, 139–146.
73 D. X. West and M. Palaniandavar, *Inorg. Chim. Acta*, 1983, **77**, L97–L98.
74 U. Sakaguchi and A. W. Addison, *J. Chem. Soc., Dalton Trans.*, 1979, 600–608.
75 I. M. Procter, B. J. Hathaway and P. Nicholls, *J. Chem. Soc. A*, 1968, 1678–1684.
76 E. Turkkan, U. Sayin, N. Erbilen, S. Pehlivanoglu, G. Erdogan, H. U. Tasdemir, A. O. Saf, L. Guler and E. G. Akgemci, *J. Organomet. Chem.*, 2017, **831**, 23–35.
77 B. J. Hathaway, Copper, in *Comprehensive Coordination Chemistry*, Pergamon Press, Oxford, 1987, vol. 5, p. 533.
78 R. P. John, A. Sreekanth, V. Rajakannan, T. A. Ajith and M. R. P. Kurup, *Polyhedron*, 2004, **23**, 2549–2559.
79 D. B. Rorabacher, *Chem. Rev.*, 2004, **104**, 651–697.
80 V. K. Bhardwaj, N. A. Alcalde, M. Corbella and G. Hundal, *Inorg. Chim. Acta*, 2010, **363**, 97–106.
81 K. Güçlü, K. Sözgen, E. Tütem, M. Ö. Zyürek and R. Apak, *Talanta*, 2005, **65**, 1226–1232.
82 D. Jiang, X. Li, L. Liu, G. B. Yagnik and F. Zhou, *J. Phys. Chem. B*, 2010, **114**, 4896–4903.
83 R. D. Patil and S. Adimurthy, *Adv. Synth. Catal.*, 2011, **353**, 1695–1700.
84 G. Battaini, A. Granata, E. Monzani, M. Gullotti and L. Casella, Biomimetic oxidations by dinuclear and trinuclear copper complexes, in *Advances in Inorganic Chemistry*, ed. R. van Eldik and J. Reedijk, Academic Press, 2006, pp. 185-233.
85 D. L. Reger, A. E. Pascui, M. D. Smith, J. Jezierska and A. Ozarowski, *Inorg. Chem.*, 2012, **51**, 11820–11836.

86 A. Jana, N. A. Alcalde, E. Ruiz and S. Mohanta, *Inorg. Chem.*, 2013, **52**, 7732–7746.
87 J. S. Woertink, L. Tian, D. Maiti, H. R. Lucas, R. A. Himes, K. D. Karlin, F. Neese, C. Wurtele, M. C. Holthausen, E. Bill, J. Sundermeyer, S. Schindler and E. I. Solomon, *Inorg. Chem.*, 2010, **49**, 9450–9459.
88 R. L. Peterson, J. W. Ginsbach, R. E. Cowley, M. F. Qayyum, R. A. Himes, M. A. Siegler, C. D. Moore, B. Hedman, K. O. Hodgson, S. Fukuzumi, E. I. Solomon, K. D. Karlin and J. Am, *Chem. Soc.*, 2013, **135**, 16454–16467.
89 M. K. Panda, M. M. Shaikh, R. J. Butcher and P. Ghosh, *Inorg. Chim. Acta*, 2011, **372**, 145–152.
90 F. Sama, A. K. Dhara, M. N. Akhtar, Y. C. Chen, M. L. Tong, I. A. Ansari, M. Raizada, M. Ahmad, M. Shahid and Z. A. Siddiqi, *Dalton Trans.*, 2017, **46**, 9801–9823.
91 M. Murali, V. Sathya, B. Selvakumaran and J. Biol, *Inorg. Chem.*, 2021, **26**, 67–79.
92 S. Adhikari, A. Banerjee, S. Nandi, M. Fondo, J. S. Matalobos and D. Das, *RSC Adv.*, 2015, **5**, 10987–10993.
93 S. Y. Shaban, A. M. Ramadan, M. M. Ibrahim, F. I. E. Shami and R. V. Eldik, *Inorg. Chim. Acta*, 2019, **486**, 608–616.
94 F. T. Ferre, J. A. L. C. Resende, J. Schultz, A. S. Mangrich, R. B. Faria, A. B. Rocha and M. Scarpellini, *Polyhedron*, 2017, **123**, 293–304.
95 A. Terán, A. Jaafar, A. E. S. Pelaez, M. C. Torralba, Á. Gutiérrez and J. Biol, *Inorg. Chem.*, 2020, **25**, 671–683.
96 C. Eicken, F. Zippel, K. B. Karentzopoulos and B. Krebs, *FEBS Lett.*, 1998, **436**, 293–299.
97 A. Rompel, H. Fischer, D. Meiwes, K. B. Karentzopoulos, A. Magrini, C. Eicken, C. Gerdemann and B. Krebs, *FEBS Lett.*, 1999, **445**, 103–110.
98 J. Mukherjee and R. Mukherjee, *Inorg. Chim. Acta*, 2002, **337**, 429–438.